THE JOURNAL OF PHYSICAL CHEMISTRY C
A JOURNAL OF THE AMERICAN CHEMICAL SOCIETY

pubs.acs.org/JPCC

Article

Formation of 2D-Structured InSe Ceramics from Amorphous Phase Deposited on a Kapton Foil

Roman Svoboda,* Lenka Durčíková, Jan Přikryl, Keisuke Hamano, Paul J. Fons, and Milos Krbal

Cite This: *J. Phys. Chem. C* 2023, 127, 16132−16147

Read Online

ACCESS | Metrics & More | Article Recommendations | Supporting Information

ABSTRACT: The formation kinetics of the 2D-layered InSe crystalline phase in thin amorphous InSe films was studied by means of differential scanning calorimetry, Raman spectroscopy, X-ray diffraction analysis, and X-ray absorption spectroscopy. All measurements were performed on as-deposited films (thicknesses ranging between 200 and 1500 nm), with Kapton foil used as a substrate. In the films with thickness ≥ 1000 nm, the formation was found to proceed via two steps: the exothermic reorganization of the amorphous phase (activation energy of 420 kJ·mol^{-1}), followed by the exothermic formation of the crystalline phase (activation energy of 227 kJ·mol^{-1}). For InSe films with thickness ≤ 500 nm, the two processes merged, but their reaction mechanism was still found to consist of two sequential phase transformations, with the reorganization in the amorphous phase being the necessary preliminary step. Both kinetic processes were found to be slowed down by the presence of mechanical defects and by the surface/interface imperfections. The possibility of two-step preparation of ideally layered flexible 2D InSe ceramics is suggested based on the separated high-temperature amorphous phase reorganization, followed by a low-temperature crystal growth step (during which excellent 2D InSe layering could be achieved).

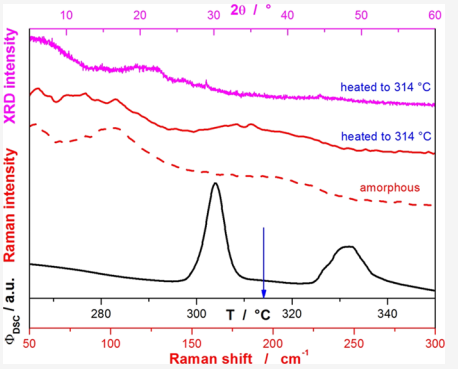

1. INTRODUCTION

Indium selenide (InSe) has recently become a major focus of research on 2D semiconducting materials.[1] The structure of 2D materials is characterized by strong chemical bonds within the layer and weak van der Waals bonds between neighboring layers. This type of atomic arrangement leads to a reduction in the importance of thermal processes and interface lattice mismatch in the growth of heterostructures in the absence of dangling bands, leading to the reduced scattering of carriers.[2−7] The popularity of InSe lies in its practically ideal bond saturation in the absence of dangling bonds,[8] ultra-high intrinsic electron mobility (up to 1000 cm^2·V^{-1}·s^{-1}),[9] and small effective electron mass. In addition, the adjustable band gap (by means of variable layering) of InSe allows the optimization of the photoelectric response as well as nonlinear absorption and refraction properties.[10,11] Indium selenide also has very good mechanical properties, exhibiting excellent flexibility and Young's modulus of ∼23[12] (an order of magnitude lower than that of the majority of similar 2D materials, only comparable to GaTe, Bi_2Se_3, and Bi_2Te_3[13−15]). Also noteworthy is the robust piezoelectric response and the excellent thermoelectric performance of InSe.[16−19]

Considering the aforementioned unique properties, InSe has great potential for numerous novel applications. In the field of photosensing devices, the large optical absorption and nonlinear optical effects of 2D multilayered InSe can be utilized for the fabrication of photoconductors,[20−22] phototransistors,[23−25] self-powered photodetectors[26−28] as well as avalanche photodetectors.[29−31] The piezoelectricity and high carrier mobility of InSe is highly beneficial for the fabrication of field-effect transistors (FET) and artificial synapses.[32−35] A particularly interesting finding was that from refs 36, 37 where an InSe transistor fabricated on a PMMA/SiO_2 dielectric bilayer showed 2 orders of magnitude increase in field-effect mobility due to the screening of interfacial Coulomb impurities and surface polar phonon scattering at an oxidized dielectric interface. The piezoresistivity and piezopotential of InSe have also been utilized for the construction of strain and pressure sensors;[38,39] the interaction of a 2D InSe structure with gases was used for the construction of a NO_2 detector;[40,41] and the electronic properties of InSe can be even utilized in memory and artificial synapse devices.[42−44] Last, but not the least, 2D-layered InSe appears to be highly efficacious for the construction of highly efficient ternary solar cells based on the polymeric PBDB-T:ITIC blend films.[45]

For the applications of 2D materials, the structural parameters (layer ordering, intralayer distance, purity, etc.) are of paramount importance. The synthesis of ideally 2D-

Received: May 19, 2023
Revised: July 26, 2023
Published: August 8, 2023

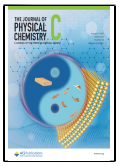

layered InSe material may be challenging, considering the complicated In−Se phase diagram,[46] the number of InSe polymorphic phases (β, γ, and ε),[1,45] and the sensitivity of InSe to ambient conditions.[1,47] Despite the 2D-functional InSe films being formed almost exclusively by the crystallization of the amorphous phase, there are only few, rather qualitative, reports on the actual crystal growth kinetics during the heat-induced amorphous-to-crystalline transformation.[48,49] This may be due to the inability to accurately measure/record the in situ crystallization process for the as-deposited thin films. Note that the most common way to study the crystallization kinetic measurements is to employ differential scanning calorimetry (DSC)[50] for films scraped off of a substrate. However, the removal of the substrate/film interface and the possible introduction of mechanically induced defects[51] may significantly alter the subsequently observed nucleation and growth rates, or even change the preferentially formed crystalline phase.

Recently, the methodology for DSC measurements of as-deposited thin films with increased accuracy was introduced.[52] This method introduced the concept of the stacking of carefully selected and preprocessed substrates (e.g., white glass, polymeric foils, mica, and so forth) with the as-deposited thin films in the DSC pan, allowing sufficient film mass to obtain a reliable heat flow signal but, at the same time, not altering the film uniformity and structure. In addition, the method employs a regular heat-flow DSC system (benefiting the well-performing verified features of a commercial high-end instrument), the calibration of which is accustomed to a specific type of the sample with low thermal conductivity. Based on this type of measurement, it was found that the substrate physicochemical properties are critical for the nucleation and crystal growth processes occurring in the observed chalcogenide thin films.[52−54] In the present paper, we will focus on the kinetics of the crystalline phase formation in an amorphous InSe thin film deposited on Kapton foil (poly-[4,4′-oxydiphenylene-pyromellitimide]). Although the fabrication of the 2D-layered InSe structure on the polymeric material can be directly related to the latest emerging hi-tech applications (flexible electronics and optoelectronics,[55,56] polymeric solar cells,[57,58] and polymer capping of the InSe layer in FETs), no information about the crystal growth rate associated with the formation of the 2D InSe crystalline phase has been published. In addition to reporting on the InSe crystallization kinetics for films deposited on a polymeric Kapton foil, these findings will be further compared to the data obtained by traditional DSC techniques using the material scraped off from an InSe thin film grown on a substrate. The crystallization behavior was studied for InSe thin films with thicknesses in the 200−1500 nm range.

2. EXPERIMENTAL SECTION

A standard melt-quench method was used to prepare a polycrystalline $In_{48}Se_{52}$ ingot from the pure elements: In (5 N, Hi-Chem, pellets) and Se (5 N, Hi-Chem, pellets). Elements were placed in a fused silica ampoule, which was evacuated to 10^{-3} Pa, sealed, and heated to 900 °C for 24 h in a rocking furnace. An ampoule with the melt was slowly cooled in air, and the formed polycrystalline ingot was cut into the form of a cylindrical target for pulsed laser deposition (PLD). The Se-rich $In_{48}Se_{52}$ target was designed to obtain thin films with the stoichiometric InSe composition. Amorphous InSe thin films with thicknesses (d_f) of 200, 500, 1000, and 1500 nm (±2%) were deposited by pulsed laser deposition in an off-axis geometry using a KrF laser (Lambda Physik COMPex 102) with the wavelength of 248 nm, pulse length of 30 nm, laser frequency of 5 Hz, and laser output intensity of 2.1 J·cm^{-2}. The deposition rate was 0.22 nm·s^{-1}. The distance between the target and the substrate holder was approx. 5 cm. Planetary rotation of the substrates in the PLD chamber ensured the structural and compositional homogeneity as well as constant d_f for the deposited films. DuPont Kapton HN foil and standard soda-lime microscopic slides (the main components being SiO_2, Na_2O, and CaO) were used as substrates and were kept at room temperature. Prior to opening the PLD chamber, the deposited films were maintained under vacuum for additional 2 h to cool and relieve stress. While the InSe films deposited on the Kapton foil were used in the as-prepared state, the films deposited onto the soda-lime substrates were scraped off (powdered) with a razor blade.

The crystal growth of both InSe sample types (as-deposited films on the Kapton foil and powdered InSe films scraped off of soda-lime substrates) was studied using DSC, using a Q2000 calorimeter (TA Instruments, USA) equipped with a cooling accessory, an autolid, an autosampler, and T-zero technology. In the case of InSe films deposited onto Kapton foil substrates, they were carefully cut into rectangular strips and stacked into hermetically sealed low-mass T-zero aluminum pans. Approx. 5−20 pieces were used for each measurement (depending on the film d_f and experimental conditions) to maintain a satisfactory signal-to-noise ratio for the measurement of the heat associated with the crystallization process. The influence of preprocessing (cutting and stacking) on the quality of the InSe film was checked by means of optical microscopy−−no cracks were observed, and the portion of mechanically damaged film (basically film edges) was estimated to be <0.1%. The measurements of the InSe powder (material scraped off of the soda-lime substrates) were performed for masses ∼0.3 ± 0.1 mg, accurately weighed to 0.01 mg. The crystallization measurements were performed using the linear heating rates q^+ of 1, 2, 5, 10, and 20 °C·min^{-1} in the 150−370 °C temperature range. Usage of the DSC autosampler enabled all the measurements to be completed within hours (rather than days) from the deposition, eliminating the danger of their long-term storage oxidation or heat−/light-induced nucleation/crystallization. The capacity of the autosampler also allowed for extensive repeatability checks that confirmed the reproducibility of the film's thermokinetic characteristics.

Apart from DSC, XRD (Empyrean Malvern Panalytical) was used to characterize the amorphous and crystallized (in DSC) InSe films. The XRD instrument was operated in 2-theta/omega using Bragg−Brentano geometry. Both amorphous and crystalline films were also subject to Raman spectroscopy measurements, using a DXR2 Raman microscope (Thermo Fisher Scientific), equipped with a 785 nm diode laser for excitation (laser spot size, 1.6 μm; laser intensity ranging up to 0.5 mW; 10 s per scan; 100 scans averaged) and a CCD detector. In and Se K-edge X-ray absorption spectra for the as-deposited amorphous InSe samples, and samples prepared in DSC by annealing at 300 and 350 °C, were measured in fluorescence mode using a 45° incidence geometry at beamline BL01B1 at SPring-8. XAS data were processed and fitted using the Athena and Arthemis software packages.

https://doi.org/10.1021/acs.jpcc.3c03390
J. Phys. Chem. C 2023, 127, 16132−16147

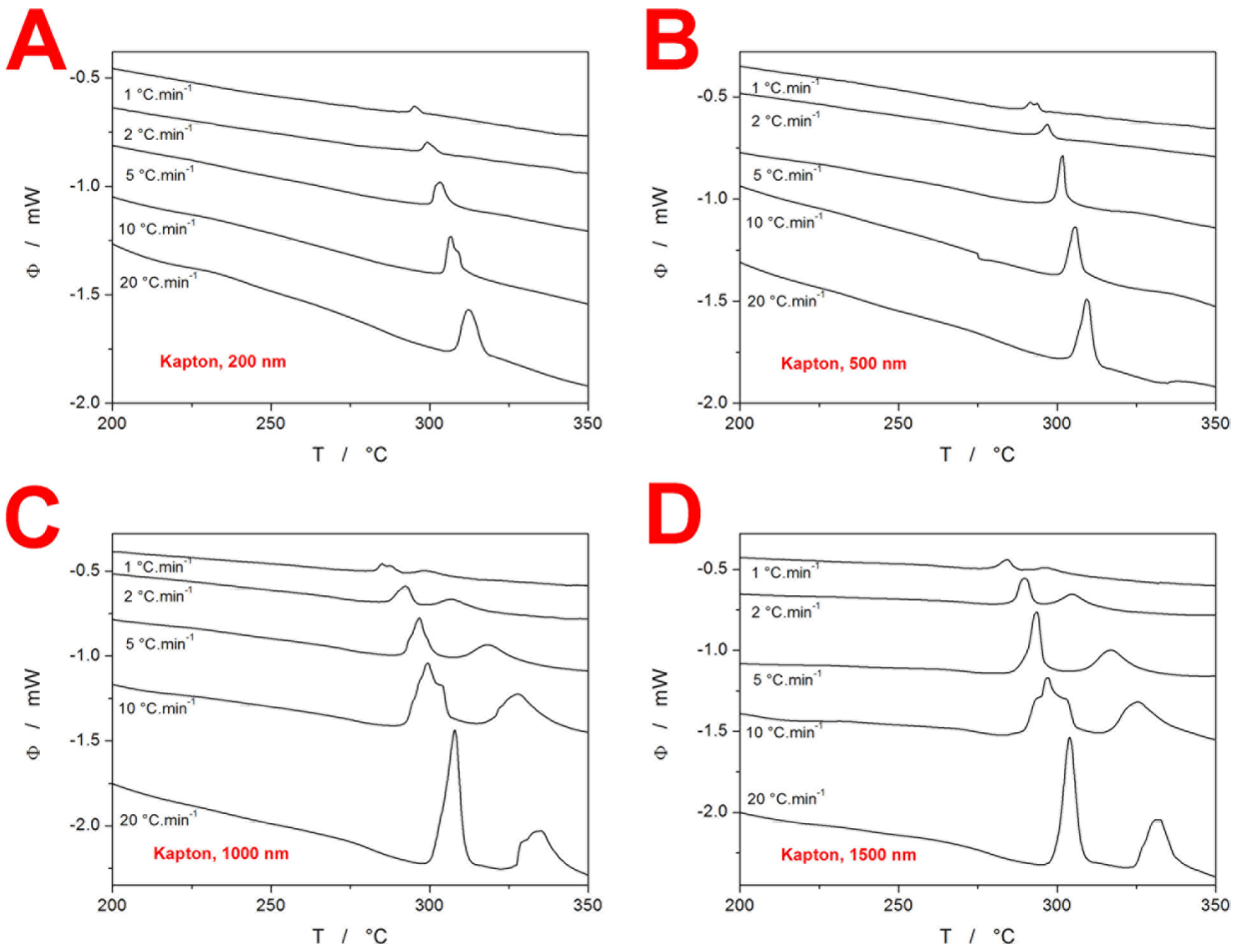

Figure 1. (A–D) DSC curves obtained for amorphous InSe thin films deposited on a Kapton foil; each graph corresponds to a different film d_f. The exothermic effects evolve in the upward direction.

3. RESULTS

The section will be split into two sub-sections, underscoring the need for complementary structural characterization measurements as a supplement to the calorimetric data.

3.1. DSC Measurements. The bulk of the present research was carried out using a DSC technique that records the heat flow Φ as a function of temperature T and/or time t (note that temperature in °C will be denoted "T", and temperature in K will be denoted "T*"). Typical DSC curves obtained for InSe amorphous films deposited on a Kapton foil are shown in Figure 1. Upon heating of the amorphous phase, the first thermally initiated phenomenon is the glass transition——a crossover between the rigid (glassy) and soft (undercooled liquid) states. For the case of InSe, the glass transition manifests itself as a simple endothermic step-like change of heat capacity in the 265–280 °C temperature range, with no associated relaxation peak (note that the effect at 275 °C on the 10 °C·min^{-1} curve in Figure 1B is a baseline twitch, not a glass-transition effect). This indicates the so-called strong confirmation of Angell's fragility concept,[59] an event that is usually connected with only tenuous relaxation movements.[60] The observation of a glass transition during the heating process was closely followed by a sharp exothermic signal corresponding to an (supposedly, the exact nature of the exothermic effects will be explored later in the article) amorphous-to-crystalline transformation. As can be seen, the crystallization signal is complex, consisting of two separate crystallization peaks. Interestingly, the second crystallization peak decreases in magnitude with d_f——and is only just recognizable for the case of the 500 nm film, with no evidence of a second crystallization peak present for the 200 nm film. Note that the crystallization peaks occasionally exhibit an irregular shape, which is a consequence of the sample stacking; as shown by the repeated measurements, the position of the peaks remains unchanged regardless of the shape. The melting of InSe occurs at ∼611 °C,[61] i.e., outside of the standard DSC measurement range.

DSC observations of powdered InSe (films scraped off the soda-lime substrate) are shown in Figure 2. The glass-transition and crystallization DSC peaks for powdered InSe occur in a similar temperature range as for the films deposited on the Kapton foil. However, there are two differences apparent between the two types of InSe samples: the crystallization of the powdered InSe manifests itself through significantly smoother DSC peaks (i.e., the morphological quality of the powdered film and the thermal gradients within the DSC pan are more uniform compared to the case of stacked samples), and the second crystallization peak is less pronounced for powdered InSe. Note that only three DSC measurements of the powdered 200 nm film were performed due to the less amount of the material (as dictated by its low d_f, given the geometry of the PLD chamber, and the requirement to perform parallel deposition on the Kapton foil and soda-lime substrate for each d_f).

https://doi.org/10.1021/acs.jpcc.3c03390
J. Phys. Chem. C 2023, 127, 16132–16147

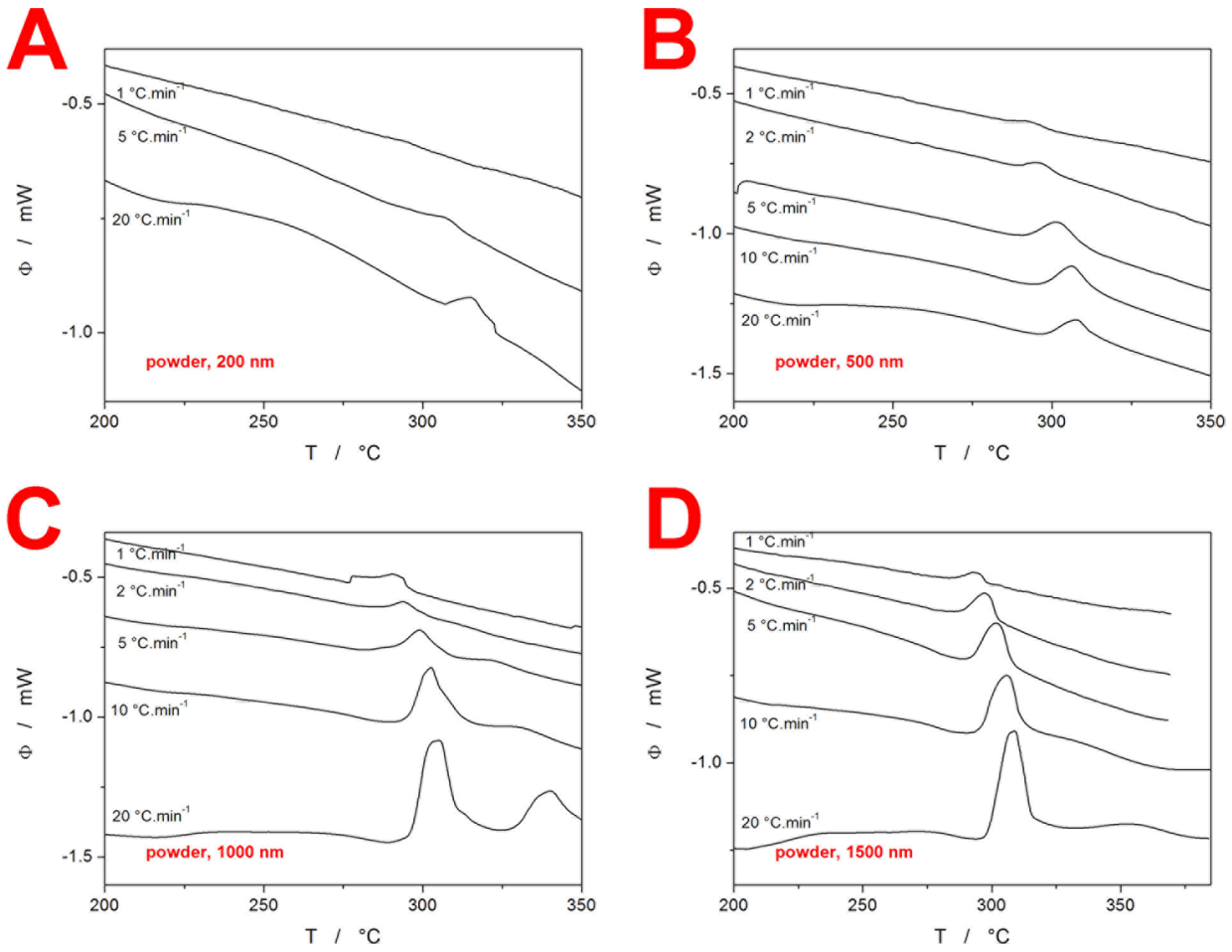

Figure 2. (A–D) DSC curves obtained for amorphous InSe thin films deposited on soda-lime substrates and subsequently scraped off; each graph corresponds to a different original film d_f. The exothermic effects evolve in the upward direction.

A direct comparison of the DSC curves obtained for the two InSe sample forms is shown in Figure 3——data measured at 1 and 20 °C·min^{-1}. The curves obtained at 20 °C·min^{-1} appear similar for both sample forms; the sharper crystallization peaks in the case of films deposited on the Kapton foil are indicative of the higher uniformity of the crystallization centers present in the as-deposited film; the weaker manifestation of the secondary (high-T) crystallization peak corresponds either to the different distribution of phase/morphological crystallization centers or to a change in the crystallization mechanism (growth rate altered by experimental conditions and/or the sample form). Note that a detailed explanation of this observation will be provided in Section 4, based on structural characterization. Contrary to the DSC curves obtained at high q^+, the data for low q^+ differ markedly for both sample forms. Not only are the secondary crystallization peaks completely absent, but the position of the main/primary crystallization peak significantly shifts to higher temperatures as well.

The q^+ dependence of the characteristic temperatures (glass-transition temperature T_g, maximum of the first crystallization peak T_{c1}, maximum of the second crystallization peak T_{c2}, and melting temperature T_m[61]) evaluated for the InSe films deposited on the Kapton foil are depicted in Figure 3C. Note that the two dependences shown for each of the crystallization peaks correspond to the lower and upper limits obtained within the set of films with different d_fs. The higher thermal stability of the amorphous phase, i.e., the higher T_{c1} value, is generally found in InSe films with lower d_f. However, the overall stability of the InSe amorphous phase is poor, as is qualitatively evidenced by the crystal growth process starting immediately after the glass transition (the onset of T_{c1} is only few °C above T_g). To quantify the amorphous phase stability, the Hruby criterion K_{Hruby}[62] is often used:

$$K_H = (T_c - T_g)/(T_m - T_c) \quad (1)$$

Whereas the T_g and T_m values are usually almost independent from various experimental and measurement conditions, the crystallization process can exhibit large changes with q^+ and the sample form, atmosphere, amount of mechanically introduced defects, stress within the sample, aging, and so forth.[63−66] In addition, no consensus has been reached in the scientific community also regarding the exact determination of T_c: the onset of the peak should be technically used instead of the peak maximum (as the glassy matrix ceases to be "stable" with the first occurrence of the crystalline phase); the first occurrence of crystallites itself is however disputed as some opinions advocate for the state of the sample being fully crystalline. Note that the latter not only disregards the fact that the Hruby criterion is a measure of glass *stability*, but this approach also further complicates the interpretation of materials that do not fully crystallize or which exhibit recrystallization into multiple crystalline phases. This ambiguity of K_{Hruby} utilization thus requires the report to always state the exact conditions for which the calculation was

https://doi.org/10.1021/acs.jpcc.3c03390
J. Phys. Chem. C 2023, 127, 16132−16147

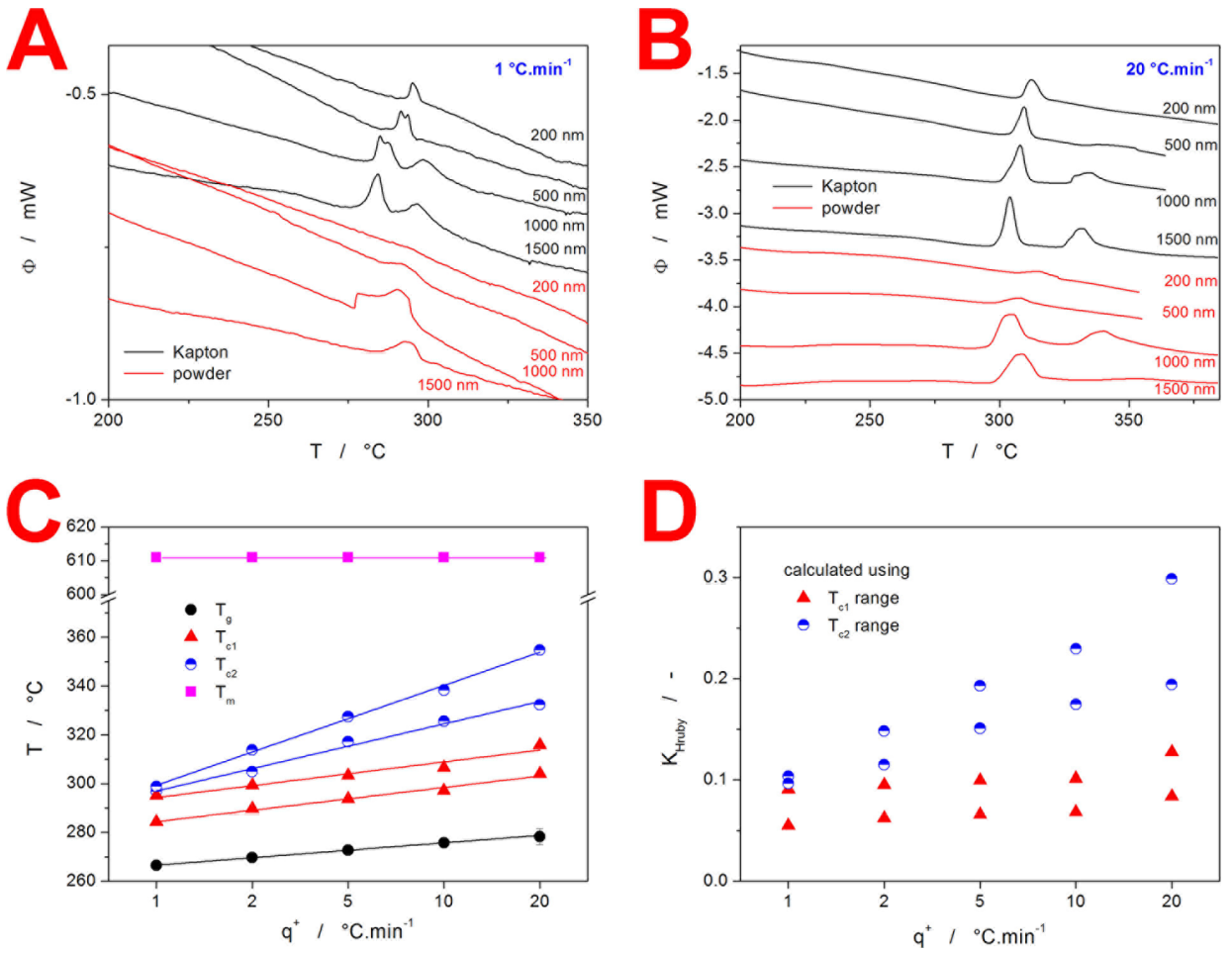

Figure 3. (A) Comparison of DSC curves obtained at 1 °C·min^{-1} for either as-deposited (on Kapton foil) or powdered (scraped off soda-lime substrates) InSe films of different d_fs'. The exothermic effects evolve in the upward direction. (B) Comparison of DSC curves obtained at 20 °C·min^{-1} for either as-deposited or powdered InSe films of different d_f's. The exothermic effects evolve in the upward direction. (C) Characteristic temperatures evaluated from the DSC data obtained for InSe thin films deposited on a Kapton foil. (D) Values of the Hruby criterion calculated from the DSC data depicted in Figure 3C.

performed.[67] For the present data, the K_{Hruby} criterion was evaluated in conformity with Figure 3C; note that the T_c values obtained for the powdered InSe films fall into the temperature ranges used for the measurements of the films deposited on the Kapton foil. As is apparent from Figure 3D, the value of K_{Hruby} can range from 0.05 to 0.3 depending only on the evaluation method. All these results indicate very low glass stability, but a comparison to the literature data should always be made with extreme caution, and the best way to use this criterion is to compare the measurements performed by the same person in a single lab.

To conclude the first subsection, the following findings have been deduced from DSC data. The complexity of the crystallization process decreases with the film d_f, with the second crystallization peak being absent for low q^+ and d_f. The powdering of the films results in a shift of the crystallization peaks to higher T and further fading of the second crystallization peak.

3.2. Structural Characterization. In the previous section, the DSC data revealed information on two important questions: (1) what is the physicochemical nature of the two crystallization peaks (i.e., what crystalline phases form); (2) what is the background for the different crystallization process manifestations for the as-deposited film and powdered material. The main instrumental technique employed to answer these questions was Raman spectroscopy. In Figure 4A, Raman spectra of the amorphous and several DSC-crystallized InSe thin films (as-deposited) on the Kapton foil are shown. Note that the DSC-crystallized samples are the samples from the measurements depicted in Figures 1 and 2, i.e., heated to 350 °C−−if not explicitly specified otherwise. The amorphous spectrum shows a typical broad band at ∼103 cm^{-1}. The majority of the InSe films deposited on the Kapton foil and crystallized in the DSC cell exhibit bands characteristic of the γ-InSe crystalline phase: A^1_{1g} at 114 cm^{-1}, E^1_{2g} at 177 cm^{-1}, A^1_{1g}(LO) at 200 cm^{-1}, E^1_{2g}(LO) at 210 cm^{-1}, and A^2_{1g} at 225 cm^{-1}.[1,36,45,68] The Raman spectra obtained for samples with slow crystallization rates are recognizably better evolved, which suggests a higher structural uniformity of the crystalline phase. All the spectra of the DSC-crystallized InSe films displayed in Figure 4A also do not show signals suggestive of the amorphous phase being present. However, the 1500 nm InSe film crystallized at 20 °C·min^{-1} exhibited additional bands at 71 and 103 cm^{-1}, which are indicative of the In_4Se_3 crystalline phase,[69,70] and a band at 84 cm^{-1}, which can be attributed to the γ-In_2Se_3 crystalline phase.[71] The presence of additional minor crystalline phases indicates the instability of the crystal growth process,[72] where under the highly

https://doi.org/10.1021/acs.jpcc.3c03390
J. Phys. Chem. C 2023, 127, 16132−16147

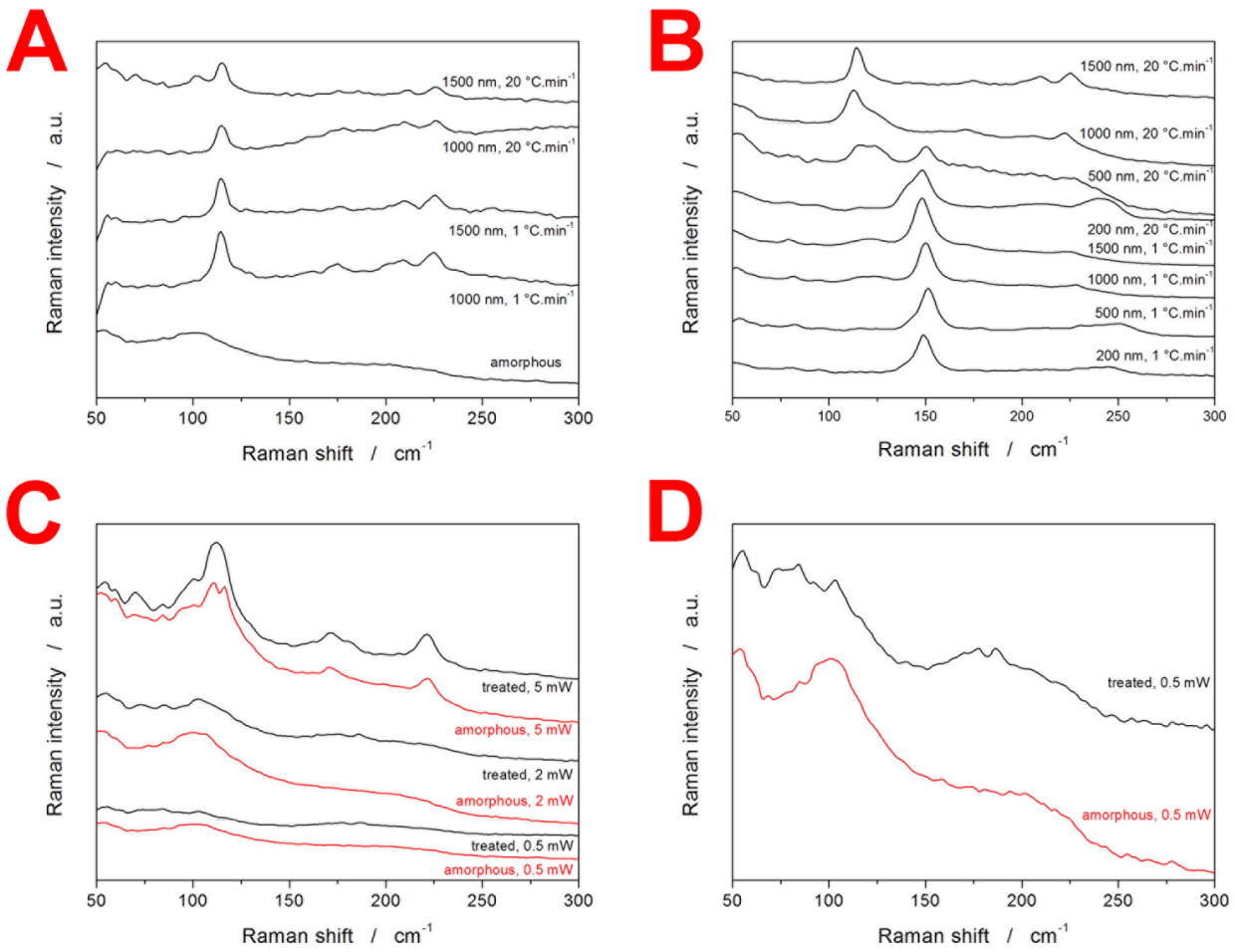

Figure 4. (A) Raman spectra of amorphous and DSC-crystallized InSe thin films deposited on a Kapton foil. The film d_f and q^+ applied during the DSC measurement are indicated. (B) Raman spectra of DSC-crystallized powdered InSe thin films. The film d_f and q^+ applied during the DSC measurement are indicated. (C) Comparison of Raman spectra obtained at different laser intensities for amorphous and treated (heated to 314 °C, i.e., above the first exothermic DSC peak) InSe films deposited on a Kapton foil. (D) Magnified Figure 4C——spectra obtained at the lowest laser intensity used are displayed.

nonequilibrium conditions (overheating associated with surplus energy during the fast heating), the kinetically preferred phases may form at the expense of the thermodynamically stable one. This is particularly relevant in the case of InSe with its complicated phase diagram,[46,73] where (instead of the formation of equimolar InSe) the amorphous structure can break down into In-rich and Se-rich domains, resulting in the preferential formation of correspondingly compositionally shifted crystallites. The Raman spectrum displayed in Figure 4A shows no bands in the 260−270 cm^{-1} range that would indicate the presence of isolated Se structures (chains and rings).[74,75] Similarly, no bands are present at 130 and 303 cm^{-1}, which would correspond to the oxidation product In_2O_3.[76] Note that the 200 and 500 nm films as-deposited on the Kapton foil and crystallized in DSC exhibited similar Raman bands as their thicker counterparts, but the signal was heavily overlaid by that of the Kapton foil.

In contrast to the InSe films deposited on the Kapton foil, the powdered InSe films exhibited a strongly q^+-dependent behavior——see Figure 4B. At a high q^+, the thickest InSe film (1500 nm) typically crystallized into the γ-InSe phase. However, already under these conditions, the dominant band at 114 cm^{-1} exhibits a weak shoulder at ∼123 cm^{-1}. This shoulder corresponds to the γ-In_2Se_3 crystalline phase formed at low temperatures (note that this phase can form even during annealing at 250 °C).[77] With the decreasing film d_f, the shoulder at ∼123 cm^{-1} increases in intensity, and for the 500 nm powdered film, new bands at 150 cm^{-1} (dominant) and 241 cm^{-1} (weak) appear——these bands are characteristic[71,78,79] of the well-developed γ-In_2Se_3 crystalline phase. For the case of low q^+, the γ-In_2Se_3 phase dominantly forms for all film d_f's. Note that for the 1500 and 1000 nm thick films, the presence of a very weak band at 227 cm^{-1} suggests traces of the InSe crystalline phase——this band is replaced by the γ-In_2Se_3 band at 241 cm^{-1} for thinner films (500 and 200 nm).

In a series of Raman measurements, the origin of the two crystallization peaks was explored, together with the resilience of the InSe films to laser-induced photo- and thermo-crystallization. The Raman spectra obtained under different laser intensities from the amorphous InSe film (1500 nm, as-deposited on the Kapton foil) and the same film heated in the DSC system just above the first kinetic peak (20 °C·min^{-1} to 309 °C, denoted as "treated") are shown in Figure 4C. At higher laser intensities (<2 mW), both films crystallize into the β-InSe phase (the missing modes at 200 and 210 cm^{-1} rule out the γ-InSe phase[71,78]). At lower laser intensities, the Raman spectra remain unaltered, revealing differences between the amorphous and treated films——see Figure 4D for a magnified

https://doi.org/10.1021/acs.jpcc.3c03390
J. Phys. Chem. C 2023, 127, 16132−16147

version of the spectrum obtained at 0.5 mW. The Raman spectra of the treated InSe films show several small bands (84, 103, 177, and 186 cm^{-1}) on an amorphous InSe background, which indicates the formation of an α-In_2Se_3 nanocrystalline phase.[71,80] No evidence of InSe Raman vibrations can be seen in the spectra of the treated films.

X-ray diffraction was used as a complementary technique to Raman spectroscopy−−see Figure 5. For the case of InSe films

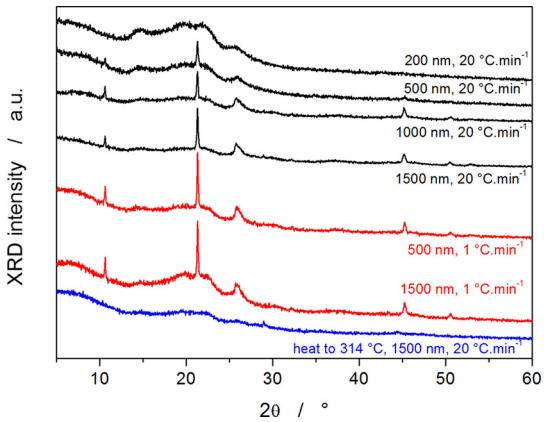

Figure 5. XRD patterns of treated and fully DSC-crystallized InSe thin films deposited on a Kapton foil. The film d_f and q^+ applied during the DSC measurement are indicated.

deposited (and crystallized) on the Kapton foil, the diffraction lines seen at 10.6, 21.2, and 45.2° 2θ are consistent with the 002, 004, and 011 planes of the γ-InSe phase.[45] The preferential orientation of these planes indicates the formation of a 2D crystalline structure. In addition to the InSe crystalline signal, the patterns display a diffuse diffraction peak at 25.8°, which may (apart from InSe with 25.4 and 25.9°) also indicate the presence of the γ-In_2Se_3 phase.[72,79] Interestingly, none of these peaks were present for the case of the treated film, i.e., the sample heated just above the first kinetic peak (to 309 °C at 20 °C·min^{-1}). The XRD pattern of the treated film was almost identical to that of the as-deposited amorphous InSe film, with only a very weak line at 28.9°, which is consistent with the formation of nanocrystalline α-In_2Se_3 (as also confirmed by Raman spectroscopy).[80] Note that the presence of additional phases (apart from InSe) was also required to describe the X-ray absorption data, as will be discussed below.

A study of the local structure by X-ray absorption (XAS) provides information on the electronic transitions around the X-ray absorption edge, as represented by XANES spectra and the coordination numbers, bond lengths, and mean-square relative displacements (determined from the Fourier-transformed EXAFS (extended X-ray absorption fine structure) data fits). Figure 6A,B shows the normalized experimental X-ray absorption spectra for both the In K- and Se K- edges, including zoomed-in figures showing oscillations right above the absorption edges. Interestingly, while the first exothermic peak at 300 °C seen on the DSC curve had a larger intensity than the second peak (see Figure 1), there were few strong differences in the shape of both the In K- and Se K-edge XANES spectra between the as-deposited amorphous InSe sample and a sample annealed at 314 °C. This finding is consistent with the XRD and Raman spectroscopy data, showing similar amorphous diffraction patterns for both states, with only very minor amount of α-In_2Se_3 crystalline phase being formed at 314 °C. In contrast, the In K- and Se K-edge XANES spectra of the annealed sample at 350 °C differ significantly from the latter XANES spectra. The insets of Figure 6A,B clearly demonstrate both the broadening of the

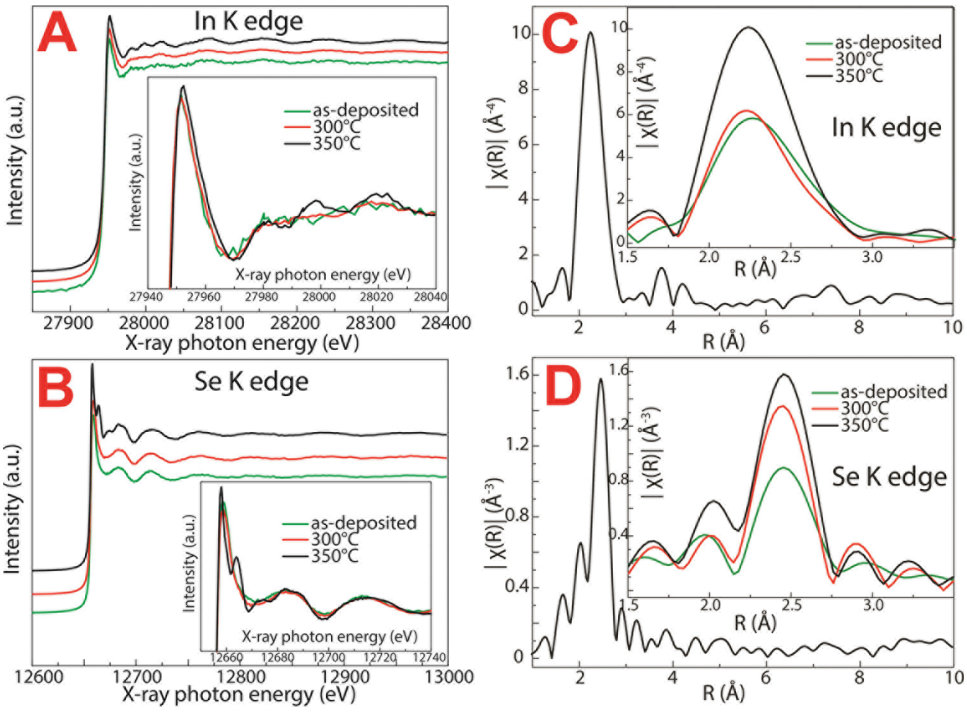

Figure 6. (A, B) Normalized experimental XANES spectra of as-deposited amorphous InSe and films annealed at 300 and 350 °C. (A) In:K-edge and (B) Se:K-edge. The inset figures show enlarged regions of the XANES spectra near the In:K- and Se:K- absorption edges. (C, D) InK- and SeK-edge Fourier-transformed spectra of as-deposited amorphous and annealed InSe at 300 and 350 °C.

https://doi.org/10.1021/acs.jpcc.3c03390
J. Phys. Chem. C 2023, 127, 16132−16147

WL InK-edge manifested by the formation of three oscillations above the absorption edge and the narrowing of WL at the Se K-edge with the formation of a new intense peak at 12,665 eV as well as a broad band in the energy range 12,669−12,700 eV, with the maximum at 12,684 eV being divided into three clearly distinguishable peaks with maxima at 12,673, 12,683, and 12,688 eV. All these unambiguous changes indicate a phase transition, which agrees well with the XRD and Raman spectroscopy data, manifested by the formation of the hexagonal InSe phase.

Figure 6C,D shows the Fourier-transformed experimental XAS data for the In K- and Se K-edges for an InSe thin film annealed at 350 °C, which was found to be in the hexagonal InSe phase. Although the InSe film annealed at 350 °C is crystalline, the second coordination shell is only clearly present at the In K-edge, while only first nearest neighbors are visible at the Se K-edge. The missing higher coordination shells may be due to the formation of a nanocrystalline fraction, crystal defects, and static or thermal disorder, since the XAS data were collected at room temperature. The insets in Figure 6C,D provide a deeper look into the evolution of the first coordination shell during the phase transition from the as-deposited amorphous InSe through the samples annealed at 300 and 350 °C, respectively. From the In site, the radial distribution function is asymmetric with a tail at a longer bond length, which may be associated with the presence of In−Se and In−In bonds.[81] After annealing amorphous InSe at 300 °C, the peak maximum shifts to lower R with a small increase in intensity, and simultaneously, the intensity of the tail region decreases for R values between 2.5 and 3 Å. Additional annealing of InSe at/above 350 °C leads to a significant increase in the intensity of the radial distribution function. The Fourier-transformed Se K-edge data show a gradual increase in the intensity of the first coordination shell of Se atoms in InSe from the as-deposited amorphous material to the crystalline phase formed during annealing at 350 °C.

To obtain information about the short-range order, we analyzed the EXAFS data measured at both edges. Real-space fitting of the Fourier-transformed EXAFS data for the In and Se K-edges was carried out simultaneously to increase the reliability of the results by reducing the number of variables fit. We assumed, in the fitting model, that the number of In−Se pairs was equal to the Se−In pairs. The fit quality at both edges and the three studied phases can be found in the Supporting Information (Figure S1); the corresponding values from the EXAFS analysis are summarized in Table 1.

The local structure of the as-deposited InSe phase consists of homopolar In−In and heteropolar In−Se bonds with coordination numbers of 0.57 and 2.63, respectively. It is important to point out that the typical uncertainty in the determination of coordination numbers is about 20%. Compared to a previous report,[81] no evidence of homopolar Se−Se bonds was observed. The overall coordination numbers were found to be 3.2 for the In edge and 2.63 for the Se edge, suggesting that In atoms are present in both pyramidal and tetrahedral coordinations, and the Se atoms exist in two- and threefold (pyramidal) coordinated structural units. The interatomic distances for In−In and In−Se were found to be 2.77 and 2.62 Å, respectively, values that are in good agreement with the literature data.[81]

The local environment of the InSe phase annealed at 300 °C is very close to that of the as-deposited InSe, with the coordination numbers for In−In pairs being 0.72 and In−Se pairs being 2.70. To achieve the best quality fit, however, additional In−Se (2) paths had to be included with the corresponding coordination number fit of 0.95 ± 0.49 with a bond length of 2.81 Å. This longer In−Se distance is attributable to the In−Se bond length present in the crystalline In_2Se_3 phase,[82] which agrees well with our results from XRD and Raman spectroscopy.

The local structure of InSe annealed at 350 °C, in contrast, clearly satisfies the hexagonal InSe phase.[83] The coordination numbers obtained, 3.98 for the In edge and 2.90 for the Se edge, confirm that In atoms exclusively form tetrahedral units and Se atoms pyramidal units. Surprisingly, the interatomic distances do not change during the phase transition from the amorphous to the crystalline InSe phase. The mean-square relative displacement (MSRD) corresponds to static and thermal disorder. One can see from Table 1 that the MSRD value is the largest for amorphous InSe (0.0067), which gradually decreases with the increasing annealing temperatures of 300 and 350 °C to 0.0043 and 0.0037, respectively. These findings indicate that the crystallization of amorphous InSe is associated with a decrease in the static disorder, which was also observed in InSb.[84]

Table 1. Coordination Numbers (CN), Bond Lengths (BL), and Mean-Square Relative Displacement (MSRD) of As-Deposited and Crystallized InSe at 300 and 350 °C

as-dep	CN	BL/Å	MSRD/Å^2
In−In	0.57 ± 0.21	2.77 ± 0.02	0.0022 ± 0.0025
In−Se	2.63 ± 0.15	2.62 ± 0.01	0.0067 ± 0.0005
Se−In	2.63 ± 0.15	2.62 ± 0.01	0.0067 ± 0.0005
Se−Se			
300 °C			
In−In	0.72 ± 0.25	2.79 ± 0.02	0.0021 ± 0.0033
In−Se	2.70 ± 0.3	2.62 ± 0.01	0.0043 ± 0.0008
Se−In	2.70 ± 0.3	2.62 ± 0.01	0.0043 ± 0.0008
In−Se (2)	0.96 ± 0.49	2.81 ± 0.02	0.0015 ± 0.0047
Se−In (2)	0.96 ± 0.49	2.81 ± 0.02	0.0015 ± 0.0047
Se−Se			
350 °C			
In−In	1.08 ± 0.24	2.77 ± 0.02	0.0009 ± 0.0044
In−Se	2.90 ± 0.15	2.62 ± 0.01	0.0037 ± 0.0003
Se−In	2.90 ± 0.15	2.62 ± 0.01	0.0037 ± 0.0003
Se−Se			

4. DISCUSSION

The amorphous phase is intrinsically interlinked with two physicochemical phenomena: the glass transition (the transformation between the kinetically frozen-in glassy structure and mobile undercooled liquid in kinetic equilibrium) and cold crystallization (the heating-induced transformation from the thermodynamically unstable amorphous phase into the thermodynamically stable crystalline phase). The primary motivation to investigate the kinetics of these processes is to enable predictions of the stability of the material (during long-term storage or material processing) and to enable the controlled formation of the crystalline phase (crucial for ceramics and glass−ceramics applications).

Starting with the structural relaxation kinetics, this process is conventionally described in terms of the phenomenological Tool−Narayanaswamy−Moynihan (TNM) model:[85−87]

https://doi.org/10.1021/acs.jpcc.3c03390
J. Phys. Chem. C 2023, 127, 16132−16147

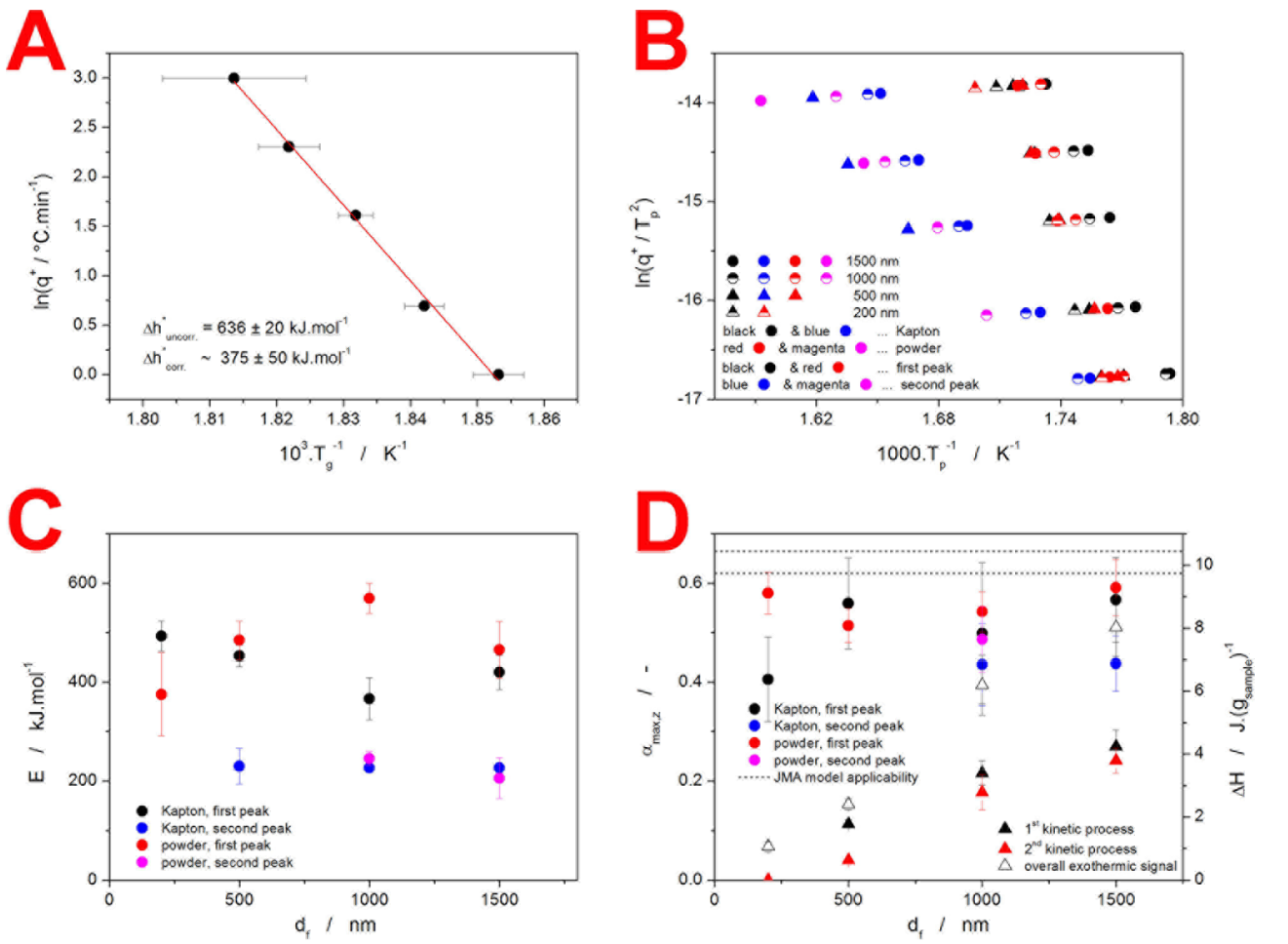

Figure 7. (A) Evaluation of uncorrected Δh^* obtained from simple heating scans of InSe thin films deposited on a Kapton foil. The Δh^* value corrected according to [x] is indicated. (B) Kissinger plot for the two DSC kinetic peaks recorded for the as-deposited and powdered InSe thin films. (C) Activation energy calculated from Figure 7B using eq 7. (D) Left axis shows $\alpha_{max,z}$ values determined for the two DSC kinetic peaks recorded for as-deposited and powdered InSe thin films. The horizontal dashed lines indicate the applicability range for the nucleation growth JMA model. The right axis indicates the averaged specific enthalpies calculated for the exothermic DSC signals measured for the InSe films deposited on the Kapton foil.

$$C_p^{red} = \frac{dT_f}{dT^*} = \frac{C_p - C_{pg}}{C_{pl} - C_{pg}} \tag{2}$$

$$C_p^{red} = \exp\left[-\left(\int_0^t \frac{dt}{\tau(T^*,T_f)}\right)^{\beta}\right] \tag{3}$$

$$\tau(T^*,T_f) = A_{TNM}\cdot\exp\left[x\frac{\Delta h^*}{RT^*} + (1-x)\frac{\Delta h^*}{RT_f}\right] \tag{4}$$

where T_f is the fictive temperature in K (corresponding to the structural state of the relaxing glass), τ is the relaxation time, Δh^* is the apparent activation energy of the structural relaxation, A is the pre-exponential constant, x is the nonlinearity parameter ($0 < x \leq 1$), and β is the nonexponentiality parameter ($0 < \beta \leq 1$). The fictive temperature is used to calculate the normalized heat capacity C_p^{red} via the extrapolation of C_{pl} and C_{pg} (the material heat capacities in the undercooled liquid and glassy states, respectively). As the glass-transition signal does not exhibit any recognizable relaxation peak, only the activation energy Δh^* can be determined based on the present data. Normally, one would utilize the so-called constant-ratio (CR) DSC cyclic experiments[88] to determine Δh^* in accordance with the methodology introduced in ref 89. However, the present material is not stable enough for several CR cycles to be performed——cycling through T_g would result in material degradation due to the close proximity of the first kinetic peak. Hence, a different procedure for the estimation of Δh^* based upon the heating scans of the as-deposited material is required. This procedure is generally not utilized,[90,91] as the material history and the associated state of low-T structure are not known, leading to Δh^* calculated using the standard approach[92] to be variable (dependent on previous thermal history) and not a material constant. However, the findings introduced in ref 91 can be used to reverse-engineer the estimation of true Δh^* with the knowledge of x and β. For the case of the present data, the nonexponentiality TNM parameter β is very small, as evidenced by the lack of a relaxation peak——the large distribution of relaxation times associated with low β results in the glass-transition effect being spread over a broader temperature interval——with no major cooperation of the structural units (that would result in an abrupt change and the corresponding overshoot in C_p). The nonlinearity TNM parameter x must be large in the case of the

https://doi.org/10.1021/acs.jpcc.3c03390
J. Phys. Chem. C 2023, 127, 16132−16147

present data, as again evidenced by the lack of a relaxation peak−−this indicates that the amorphous InSe structure relaxes almost solely as the consequence of the temperature changes via sequences of independent structural changes, with little influence from memory effects and structure cooperation.[93] With this knowledge, the magnitudes of the systematic errors associated with the evaluation of the as-prepared materials (introduced in[91]) can be used to estimate the true Δh^* value based on the application of the standard Moynihan equation:

$$\ln(q^+) = -\frac{\Delta h^*}{RT_g} + \text{const} \tag{5}$$

The uncorrected Δh^* value determined by means of eq 5 is 636 ± 20 kJ·mol^{-1} (see Figure 7A), which is unprecedentedly high for a chalcogenide glass. The Δh^* values for chalcogenide materials usually fall into the 300−450 kJ·mol^{-1} range (with very few exceptions above 500 kJ·mol^{-1}). A correction of this value based on ref 91 (in particular, Figure 4 of this reference) yields $\Delta h^*_{corr.} \approx 375 \pm 50$ kJ·mol^{-1}, a value consistent with the literature data for amorphous chalcogenide materials. Note, however, that kinetic calculations aimed at predicting the q^+ dependence of the glass-transition position can still be performed using the 636 kJ·mol^{-1} value, as the linearity and consistency of the raw data in Figure 7A are sufficient.

Moving on to the exothermic kinetic peaks, these types of solid-state transformations are commonly described in terms of the basic kinetic equation[94] (eq 6A). Note that this equation is a product of three general equations, pairing the universal solid-state equation (eq 6B) with the expression for the autocatalytic Šesták-Berggren (AC) model[95] (eq 6C) and with the relation interconnecting the conversion rate with the DSC signal (eq 6D):

$$\Phi = \Delta H \cdot A \cdot e^{-E/RT^*} \cdot \alpha^M (1-\alpha)^N \tag{6A}$$

$$d\alpha/dt = I \cdot A \cdot e^{-E/RT^*} \cdot f(\alpha) \tag{6B}$$

$$f(\alpha)_{AC} = \alpha^M (1-\alpha)^N \tag{6C}$$

$$d\alpha/dt = \Phi/\Delta H \tag{6D}$$

where Φ is the DSC heat flow, ΔH is the enthalpy change associated with the kinetic process, A is a pre-exponential factor, E is the apparent activation energy of the kinetic process, R is the universal gas constant, T^* is temperature in K, α is the degree of conversion, $d\alpha/dt$ is the rate of conversion, I is a general expression for the area under the kinetic peak, $f(\alpha)$ is a general expression for a solid-state kinetic model, and M and N are the kinetic exponents of the empirical Šesták-Berggren (AC) model.[95] Considering the variety of asymmetries and shapes exhibited by the DSC data (see Figures 1 and 2), the flexible AC kinetic model had to be chosen as the initial option to obtain an accurate representation of the experimental data. As will be shown later, none of the relevant physically meaningful macroscopic solid-state models can describe the present data.

The standard approach, nowadays, to the kinetic analysis of the DSC crystallization data is as follows. First, the activation energy E needs to be determined, either by the linearization or the isoconversional method. Second, the applicability of the physically meaningful kinetic models needs to be either confirmed or disproved. Third, the DSC data are modeled by means of eq 6B, with the appropriate kinetic model included; in this step, the possible T or q^+ trends in kinetics need to be revealed, and the kinetic modeling needs to reflect them. If the crystallization kinetics is consistent across the explored range of the experimental conditions, the multivariate kinetic analysis[96] can be used with a proper reaction scheme implemented. If some significant kinetic trends are identified, then the single-curve multivariate kinetic analysis sc-MKA[97] with E fixed at the corresponding values is used. In the following text, this sequence will be followed.

The key quantity in eq 6A is the activation energy E, which is responsible for the changes in the process localization on the temperature axis. This quantity is usually determined by means of the linearization Kissinger method:[98]

$$\ln\left(\frac{q^+}{T_p^{*2}}\right) = -\frac{E}{RT^*} + \text{const} \tag{7}$$

where T_p^* denotes the temperature in K corresponding to the maximum of the DSC peak.

The so-called Kissinger plot for the present InSe films and powders is depicted in Figure 7B. It is immediately apparent that there is a striking difference in the slopes associated with the Kissinger dependences of the first and second kinetic processes. Applying eq 7 to the data from Figure 7B provides the E values shown in Figure 7C. Whereas the second kinetic process is characterized by $E \approx 230$ kJ·mol^{-1} (which is on the upper side of typical chalcogenide glasses but is still reasonable for the crystallization process of a chalcogenide glass), the activation energy for the first kinetic process is extremely high, reaching between 400 and 550 kJ·mol^{-1}. Such high E values are typical for solid−solid phase transformations in amorphous chalcogenides or for the crystallization of metallic or oxide glasses (crystallizing at much higher temperatures than that of InSe). Considering the presence of such a high E value for the present InSe material, the large evolution of heat associated with the first kinetic peak appears to correspond to a structural reorganization of the amorphous phase, as also suggested by the XAS, Raman spectroscopy, and XRD characterization techniques. In particular, the fundamental basis of the 2D InSe structure may be formed at the molecular level during the transformation process, together with the segregation (and the consequent crystallization into the α-In_2Se_3 phase) of Se-richer structural domains. It is also very important to bear in mind that the intensity of the second DSC peak diminishes with decreasing d_f, but the structural and morphological characteristics of the final (high-T) crystalline product remain unchanged. This unambiguously indicates that under these conditions, larger portions of the 2D γ-InSe phase are being gradually formed immediately after the short-range reorganization of the amorphous phase and also suggests that these two processes are sequential (and indirectly implies the converging course of the two types of Kissinger dependences seen in Figure 7B) and are not independent. The partition of the two processes at higher d_f also indicates that greater InSe film thickness slows down the crystallization (second) process, and progressively, a larger fraction of the 2D-layered structure forms independently, at a higher temperature. The slowdown of the crystalline phase formation may also be explained by the rigidity of the thicker InSe films, not yielding to the macroscopic bending force introduced through the difference in thermal expansion coefficients ($CTE_{Kapton} = 20 \times 10^{-6}$ °C^{-1},[99] $CTE_{InSe} = 10-17 \times 10^{-6}$ °C^{-1}[100]). This internal

https://doi.org/10.1021/acs.jpcc.3c03390
J. Phys. Chem. C 2023, 127, 16132−16147

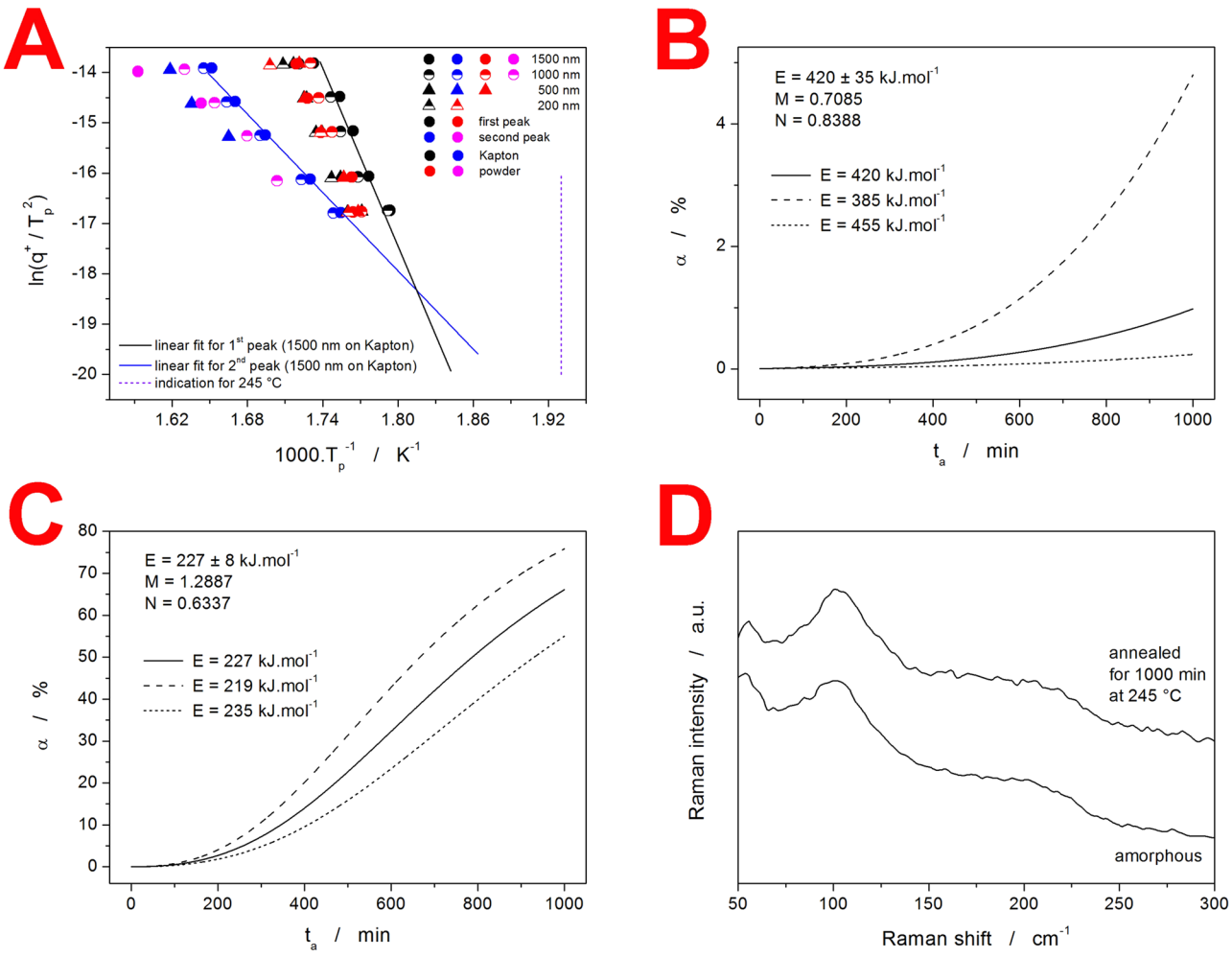

Figure 8. (A) Kissinger plot from Figure 7B with linearly extrapolated values of the first and second exothermic DSC peaks obtained for a 1500 nm InSe film deposited on a Kapton foil. The vertical dashed line indicates the temperature (245 °C) of the isothermal annealing experiment. (B, C) Kinetic prediction for the 1000 min isothermal annealing experiment carried out at 245 °C. The simulations were performed using the AC model parameters and a value for E determined by the low-q^+ (0.5 °C·min^{-1}) DSC data of the first (B) and second (C) exothermic processes exhibited by the 1500 nm InSe film deposited on a Kapton foil. The values of eqs 6A–6C used for each simulation are depicted in the corresponding graphs. The solid lines correspond to simulations utilizing the average E values; the dashed lines correspond to calculations using the average $E \pm$ standard deviation as confidence intervals. (D) Comparison of the Raman spectra of an amorphous InSe film and a sample that underwent the isothermal annealing experiment (1000 min at 245 °C).

tensile stress may be the reason for the hindered crystal growth of the highly ordered 2D layers––akin to the changes in the crystal growth behavior recently observed for Se–Te[52] and Sb_2Se_3[53] thin films.

Apart from the large difference in the slopes of the Kissinger dependences obtained for the two kinetic peaks, Figure 7B also shows the evolution of T_p*s with respect to d_f. With the decreasing film d_f, both the reorganization of the amorphous phase and the formation of the crystalline 2D InSe phase shift to (slightly) higher temperatures. Two possible explanations can be offered for this observation: (1) thinner films have a higher surface-to-volume ratio and are more prone to free-surface and interfacial defects, which can aggravate the formation of the layered 2D structure; (2) thinner films exhibit a higher degree of intermingling of the two processes involved (reorganization of the amorphous phase and the consequent formation of the crystalline phase), where the immediate concurrent formation of crystallites may disturb and retard the reorganization of the amorphous phase in the adjacent structural domains. An increase of T_p*s is also clearly apparent for the powdered InSe films, when compared to comparably thick films deposited on a Kapton foil. This can be interpreted as a consequence of mechanically induced defects introduced into the film structure during powdering––the induced fractures and mechanical stress may also be responsible for the reduction in the formation of the layered 2D structure.

As described above, the linearization Kissinger method was used in the present study to determine E and its q^+/T dependences. Another option may be the isoconversional methods,[92] which can be, however, less reliable and more difficult to interpret––especially in the case of unideal, complex, or scattered experimental data (such as the present ones). Despite the isoconversional methods being less beneficial/appropriate in the present case, the course of the dependences may be interesting to explore––the corresponding analyses are included in the Supporting Information.

Regarding the above-modeled kinetic behavior (the kinetic function "$\alpha^M(1-\alpha)^N$" in eq 6A), it is clear from Figure 1 that both exothermic peaks show asymmetry and occasionally

https://doi.org/10.1021/acs.jpcc.3c03390
J. Phys. Chem. C 2023, 127, 16132–16147

exhibit a complex behavior (split exothermic signals signifying multiple overlapping subpeaks). In such circumstances, the kinetics are first best characterized by means of the characteristic kinetic function $z(\alpha)$[101] to reveal the possible correspondence with the physically meaningful solid-state models:

$$z(\alpha) = g(\alpha)\cdot f(\alpha) \approx \Phi\cdot T^{*2} \quad (8)$$

which indicates the overall asymmetry of the kinetic signal. Note that $g(\alpha)$ is the integral form of the $f(\alpha)$ function (note that the right-hand side of eq 9 is missing a negligible term that is omitted for practical purposes). The degree of conversion corresponds to the maximum of the $z(\alpha)$ function, $\alpha_{max,z}$, and is a fingerprint used in numerous physically meaningful solid-state kinetic models.[92] The values of $\alpha_{max,z}$ determined for the present InSe films are shown in Figure 7D, together with the applicable range (as indicated by the dashed lines)[102] for the most common kinetic model describing the nucleation growth-based crystal formation, the Johnson−Mehl−Avrami (JMA) model.[103−106] Note that the other major physically meaningful kinetic models−−the contracting geometry, diffusion, and n^{th} order models−−are characterized by even higher values of $\alpha_{max,z}$ than the JMA model. As is apparent, the asymmetry of the InSe kinetic DSC peaks is indeed significantly more positive (as indicated by the lower value of $\alpha_{max,z}$) than that of the physically meaningful models, resulting here in the usage of the empirical AC model (eqs 6A−6C). Considering the magnitude of the error bars associated with the datapoints ($\alpha_{max,z}$ values were averaged over all applied q^+), both the evaluated kinetics (reorganization of the amorphous phase and the growth of the 2D InSe crystalline phase) are reasonably uniform, suitable for potential predictions of the kinetic course of the corresponding physicochemical processes.

In addition to the $\alpha_{max,z}$ values, Figure 7D also displays the enthalpy changes associated with the two exothermic kinetic processes, as recorded on the DSC curves obtained for InSe films deposited on the Kapton foil. The evolved heat is referred to the overall sample mass, i.e., the Kapton + InSe film. The film mass is negligible compared to that of the underlying Kapton foil, but both masses are proportional via the shared overall area of the samples input into the DSC pan; note that only the samples of the Kapton foil fully covered with the InSe film were measured. Therefore, one would expect a linear relationship (with the dependence going through the 0/0 coordinate) between d_f and the overall ΔH calculated as a sum of both exothermic peaks: if the fundamental nature of the process remains unchanged, the released/consumed specific heat should remain constant. This assumption is fully supported by the experimental data, as displayed in Figure 7D. On the other hand, the same is not valid for each of the two exothermic peaks, when evaluated separately. The intercepts of the two supposedly linear models are not equal to 0. In comparison with the overall ΔH−d_f dependence, this unambiguously confirms that the second kinetic peak gradually merges with the first as d_f decreases.

The main reason for determining the formal solid-state kinetics is to predict the kinetic behavior under extrapolated experimental conditions (usually at lower T, where the experimental kinetic data are difficult or impossible to obtain). In practice, kinetic predictions can be used to determine qualities such as the long-term stability of the material, the acceptable conditions for material processing, and/or the time/temperature program for the preparation of ceramics and glass−ceramics from the amorphous phase. The present case of crystallite formation in an InSe thin film is very specific from the point of view of the prediction of material kinetics. Whereas the majority of joint crystallization processes is in general kinetically independent, for InSe films, the formation of the crystalline phase appears to be directly dependent on the preceding reorganization of the amorphous phase−−resulting in the dependence of the consequent reaction process in terms of formal kinetics. Since the first reaction step, the reorganization of the amorphous phase, has a large activation energy, it is expected to be the necessary preliminary kinetic step, if the two processes are truly kinetically consequent.

To verify this hypothesis, a long-term isothermal annealing experiment was performed for the 1500 nm InSe film deposited on the Kapton foil. The extrapolated Kissinger dependences of the first and second kinetic processes occurring in the sample show that at ∼278 °C (the intersection of the two extrapolated lines), the reaction rate for the two mechanisms is similar (see Figure 8A). If the two processes were independent of each other, the formation of the InSe crystalline phase would become dominant below 278 °C. To avoid ambiguity and misrepresentation, we have chosen a temperature of 245 °C (well below the intersection) for the long-term annealing experiment−−represented by the dashed vertical violet line in Figure 8A. The kinetic predictions for the 1000 min isothermal annealing at 245 °C were calculated based on the corresponding kinetic data (obtained at 0.5 °C·min^{-1} for the two kinetic peaks) using the sc-MKA (single-curve multivariate kinetic analysis) methodology.[96,97] The two kinetic equations used for these simulations (with the enumerated quantities determined by the combination of the Kissinger equation and the sc-MKA method) were:

$$d\alpha_1/dt = 10^{37.41}\cdot e^{-420{,}000/RT^*}\cdot \alpha_1^{0.709}\,(1-\alpha_1)^{0.839} \quad (9)$$

$$d\alpha_2/dt = 10^{18.63}\cdot e^{-227{,}000/RT^*}\cdot \alpha_2^{0.634}\,(1-\alpha_2)^{1.289} \quad (10)$$

Note that the indices 1 and 2 correspond to the reorganization of the amorphous structure and the consequent formation of the 2D InSe crystalline phase, respectively. The sc-MKA determination, i.e., the fits produced by the nonlinear optimization, is shown in the Supporting Information.

The kinetic prediction for the reorganization of the amorphous structure (first exothermal peak) is depicted in Figure 8B, and the prediction for the formation of the 2D InSe crystalline phase is shown in Figure 8C. In each graph, the three dependences of the degree of conversion α on the annealing time t_a are displayed. The legends in the graphs show the activation energies (taken from Figure 7C) and the AC model parameters (see eqs 6A−6C) determined by the sc-MKA method that was used for the given kinetic simulations. The simulation results for the average E values are represented by the solid lines; the dashed lines represent the confidence interval calculated using the variance represented by the E error bars. Note that E has several orders of magnitude larger influence on the kinetic predictions than other quantities; thus, the statistical variation of M and N can be neglected. The predictions in Figure 8B,C show that if the two processes were independent, the formation of the InSe crystalline phase would proceed up to 55−75% conversion, whereas the reorganization of the amorphous phase would be only a few percent from completion. Verification of the structural state of the sample after annealing was carried out by means of Raman spectroscopy (see Figure 8D). The Raman spectrum of the

https://doi.org/10.1021/acs.jpcc.3c03390
J. Phys. Chem. C 2023, 127, 16132−16147

sample annealed for 1000 min at 245 °C is practically identical to the spectrum of the amorphous InSe film, indicating that no InSe crystalline phase has formed and proving that the two processes are indeed consequent (with the reorganization of the amorphous phase being a mandatory condition for the formation of the 2D InSe crystalline phase).

5. CONCLUSIONS

The formation of the 2D-structured InSe crystalline phase was extensively studied by means of DSC, XRD, Raman spectroscopy, and XAS. Whereas the DSC heating curves of the thin amorphous InSe films deposited on the Kapton foil exhibit the manifestation of two neighboring exothermic kinetic processes (exothermic signals are usually attributed to the amorphous-to-crystalline transformation), the temperature-resolved XRD and Raman spectroscopy data reveal that the first kinetic process is associated solely with the changes in the amorphous phase. The very high activation energy (akin to that of the glass transition) determined for the DSC data corresponding to the first kinetic peak also suggests that the transformation mechanism relates to the structural (dis)order of the amorphous phase. In fact, the close vicinity of T_g and the first kinetic peak may indicate that the glass transition (resulting in a loosened and more reactive liquid-like structure) can be an initiator for the exothermic structural reordering. The large enthalpy change characterizing the first kinetic process together with the XAS results (indicating a homogeneous distribution of the bonding arrangements) confirms that the first kinetic process occurs in the whole volume of the amorphous InSe thin films and involves a major rearrangement of the amorphous structure. Based on these observations, the first kinetic process is most probably associated with the fundamental basis of the formation of the layered 2D InSe structure, which is only in the second step, followed by the formation of a true long-range-ordered crystalline structure.

A detailed kinetic analysis of the DSC crystallization data has shown that the reordering of the amorphous phase as well as the consequent crystal growth of the InSe phase is hindered by the presence of mechanical defects and by the surface/interface imperfections (increasingly introduced via the lowered volume/surface ratio of the thinner films). The kinetic predictions based on the basic kinetic equation with the Sestak−Berggren model have allowed the determination of the reaction mechanism, confirming that the two processes are indeed consequent, with the reorganization in the amorphous phase being the necessary preliminary step. Due to the very high activation energy of this step, both processes essentially merge at low q^+ and/or T. On the other hand, the separation of the two processes achieved at high q^+ offers an interesting possibility of a two-step preparation process for ideally layered flexible 2D InSe ceramics: In the first step, the thin film would be shortly heated (285 °C for 2 min) to complete the reordering of the amorphous phase. In the second step, the formation of InSe ceramics could be controlled solely based on the crystal growth process kinetics−−e.g., via annealing at significantly lower T.

■ ASSOCIATED CONTENT

Supporting Information

The Supporting Information is available free of charge at https://pubs.acs.org/doi/10.1021/acs.jpcc.3c03390.

Analysis of the EXAFS data; evaluation of activation energy by isoconversional methods; and fits of the DSC data using the sc-MKA method (PDF)

■ AUTHOR INFORMATION

Corresponding Author

Roman Svoboda − *Department of Physical Chemistry, Faculty of Chemical Technology, University of Pardubice, 532 10 Pardubice, Czech Republic;* orcid.org/0000-0002-1253-366X; Phone: +420 466 037 346; Email: roman.svoboda@atlas.cz

Authors

Lenka Durčíková − *Center of Materials and Nanotechnologies (CEMNAT), Faculty of Chemical Technology, University of Pardubice, 530 02 Pardubice, Czech Republic*

Jan Přikryl − *Center of Materials and Nanotechnologies (CEMNAT), Faculty of Chemical Technology, University of Pardubice, 530 02 Pardubice, Czech Republic*

Keisuke Hamano − *Department of Electronics and Electrical Engineering, Faculty of Science and Technology, Keio University, Yokohama, Kanagawa 223-8522, Japan*

Paul J. Fons − *Department of Electronics and Electrical Engineering, Faculty of Science and Technology, Keio University, Yokohama, Kanagawa 223-8522, Japan;* orcid.org/0000-0002-7820-1924

Milos Krbal − *Center of Materials and Nanotechnologies (CEMNAT), Faculty of Chemical Technology, University of Pardubice, 530 02 Pardubice, Czech Republic;* orcid.org/0000-0002-8317-924X

Complete contact information is available at: https://pubs.acs.org/10.1021/acs.jpcc.3c03390

Notes

The authors declare no competing financial interest.

■ ACKNOWLEDGMENTS

This work was supported by the Czech Science Foundation (23-07574S) and The Ministry of Education, Youth, and Sports (LM2023037). The authors also acknowledge the bl01b1 XAFS beam time at Spring-8 authorized by proposal 2022A1315.

■ REFERENCES

(1) Dai, M.; Gao, C.; Nie, Q.; Wang, Q.-J.; Lin, Y.-F.; Chu, J.; Li, W. Properties, Synthesis, and Device Applications of 2D Layered InSe. *Adv. Mater. Technol.* **2022**, *7*, No. 2200321.

(2) Castro Neto, A. H.; Guinea, F.; Peres, N. M. R.; Novoselov, K. S.; Geim, A. K. The electronic properties of graphene. *Rev. Mod. Phys.* **2009**, *81*, 109.

(3) Mak, K. F.; Shan, J. Photonics and optoelectronics of 2D semiconductor transition metal dichalcogenides. *Nat. Photonics* **2016**, *10*, 216−226.

(4) Geim, A. K.; Grigorieva, I. V. Van der Waals heterostructures. *Nature* **2013**, *499*, 419−425.

(5) Novoselov, K. S.; Mishchenko, A.; Carvalho, A.; Castro Neto, A. H. 2D materials and van der Waals heterostructures. *Science* **2016**, *353*, No. aac9439.

(6) Kim, S.; Konar, A.; Hwang, W.-S.; Lee, J. H.; Lee, J.; Yang, J.; Jung, C.; Kim, H.; Yoo, J.-B.; Choi, J.-Y.; et al. High-mobility and low-power thin-film transistors based on multilayer MoS2 crystals. *Nat. Commun.* **2012**, *3*, 1011.

(7) Chuang, H. J.; Chamlagain, B.; Koehler, M.; Perera, M. M.; Yan, J.; Mandrus, D.; Tomanek, D.; Zhou, Z. Low-Resistance 2D/2D

Ohmic Contacts: A Universal Approach to High-Performance WSe2, MoS2, and MoSe2 Transistors. *Nano Lett.* **1896**, *2016*, 1896.
(8) Bandurin, D. A.; Tyurnina, A. V.; Yu, G. L.; Mishchenko, A.; Zolyomi, V.; Morozov, S. V.; Kumar, R. K.; Gorbachev, R. V.; Kudrynskyi, Z. R.; Pezzini, S.; et al. High electron mobility, quantum Hall effect and anomalous optical response in atomically thin InSe. *Nat. Nanotechnol.* **2017**, *12*, 223−227.
(9) Li, M.; Lin, C. Y.; Yang, S. H.; Chang, Y. M.; Chang, J. K.; Yang, F. S.; Zhong, C.; Jian, W. B.; Lien, C. H.; Ho, C. H.; Liu, H. J.; Huang, R.; Li, W.; Lin, Y. F.; Chu, J. High Mobilities in Layered InSe Transistors with Indium-Encapsulation-Induced Surface Charge Doping. *Adv. Mater.* **2018**, *30*, No. e1803690.
(10) Tamalampudi, S. R.; Lu, Y. Y.; Kumar, U. R.; Sankar, R.; Liao, C. D.; Moorthy, B. K.; Cheng, C. H.; Chou, F. C.; Chen, Y. T. High performance and bendable few-layered InSe photodetectors with broad spectral response. *Nano Lett.* **2014**, *14*, 2800.
(11) Pan, H.; Cao, L.; Chu, H.; Wang, Y.; Zhao, S.; Li, Y.; Qi, N.; Sun, Z.; Jiang, X.; Wang, R.; Zhang, H.; Li, D. Broadband Nonlinear Optical Response of InSe Nanosheets for the Pulse Generation From 1 to 2 μm. *ACS Appl. Mater. Interfaces* **2019**, *11*, 48281−48289.
(12) Zhao, Q.; Frisenda, R.; Wang, T.; Castellanos-Gomez, A. InSe: a two-dimensional semiconductor with superior flexibility. *Nanoscale* **2019**, *11*, 9845−9850.
(13) Chitara, B.; Ya'akobovitz, A. Elastic properties and breaking strengths of GaS, GaSe and GaTe nanosheets. *Nanoscale* **2018**, *10*, 13022−13027.
(14) Yan, H.; Vajner, C.; Kuhlman, M.; Guo, L.; Li, L.; Araujo, P. T.; Wang, H.-T. Elastic behavior of Bi_2Se_3 2D nanosheets grown by van der Waals epitaxy. *Appl. Phys. Lett.* **2016**, *109*, No. 032103.
(15) Guo, L.; Yan, H.; Moore, Q.; Buettner, M.; Song, J.; Li, L.; Araujo, P. T.; Wang, H.-T. Elastic properties of van der Waals epitaxy grown bismuth telluride 2D nanosheets. *Nanoscale* **2015**, *7*, 11915−11921.
(16) Dai, M.; Chen, H.; Wang, F.; Hu, Y.; Wei, S.; Zhang, J.; Wang, Z.; Zhai, T.; Hu, P. Robust Piezo-Phototronic Effect in Multilayer γ-InSe for High-Performance Self-Powered Flexible Photodetectors. *ACS Nano* **2019**, *13*, 7291−7299.
(17) Dai, M.; Wang, Z.; Wang, F.; Qiu, Y.; Zhang, J.; Xu, C. Y.; Zhai, T.; Cao, W.; Fu, Y.; Jia, D.; et al. Two-Dimensional van der Waals Materials with Aligned In-Plane Polarization and Large Piezoelectric Effect for Self-Powered Piezoelectric Sensors. *Nano Lett.* **2019**, *19*, 5410.
(18) Hung, N. T.; Nugraha, A. R. T.; Saito, R. Two-dimensional InSe as a potential thermoelectric material. *Appl. Phys. Lett.* **2017**, *111*, No. 092107.
(19) Hou, X.; Chen, S.; Du, Z.; Liu, X.; Cui, J. Improvement of the thermoelectric performance of InSe-based alloys doped with Sn. *RSC Adv.* **2015**, *5*, No. 102856.
(20) Luo, W. G.; Cao, Y. F.; Hu, P. G.; Cai, K. M.; Feng, Q.; Yan, F. G.; Yan, T. F.; Zhang, X. H.; Wang, K. Y. Gate Tuning of High-Performance InSe-Based Photodetectors Using Graphene Electrodes. *Adv. Opt. Mater.* **2015**, *3*, 1418.
(21) Yang, H. W.; Hsieh, H. F.; Chen, R. S.; Ho, C. H.; Lee, K. Y.; Chao, L. C. Ultraefficient Ultraviolet and Visible Light Sensing and Ohmic Contacts in High-Mobility InSe Nanoflake Photodetectors Fabricated by the Focused Ion Beam Technique. *ACS Appl. Mater. Interfaces* **2018**, *10*, 5740−5749.
(22) Hu, S.; Zhang, Q.; Luo, X.; Zhang, X.; Wang, T.; Cheng, Y.; Jie, W.; Zhao, J.; Mei, T.; Gan, X. Au−InSe van der Waals Schottky junctions with ultralow reverse current and high photosensitivity. *Nanoscale* **2020**, *12*, 4094.
(23) Cao, R.; Wang, H. D.; Guo, Z. N.; Sang, D. K.; Zhang, L. Y.; Xiao, Q. L.; Zhang, Y. P.; Fan, D. Y.; Li, J. Q.; Zhang, H. Black Phosphorous/Indium Selenide Photoconductive Detector for Visible and Near-Infrared Light with High Sensitivity. *Adv. Opt. Mater.* **2019**, *7*, No. 1900020.
(24) Wu, F.; Xia, H.; Sun, H. D.; Zhang, J. W.; Gong, F.; Wang, Z.; Chen, L.; Wang, P.; Long, M. S.; Wu, X.; Wang, J.; Ren, W.; Chen, X.; Lu, W.; Hu, W. AsP/InSe Van der Waals Tunneling Heterojunctions with Ultrahigh Reverse Rectification Ratio and High Photosensitivity. *Adv. Funct. Mater.* **2019**, *29*, No. 1900314.
(25) Qi, T.; Gong, Y.; Li, A.; Ma, X.; Wang, P.; Huang, R.; Liu, C.; Sakidja, R.; Wu, J. Z.; Chen, R.; et al. Interlayer Transition in a vdW Heterostructure toward Ultrahigh Detectivity Shortwave Infrared Photodetectors. *Adv. Funct. Mater.* **2020**, *30*, No. 1905687.
(26) Sun, Y.; Gao, W.; Li, X.; Xia, C.; Chen, H.; Zhang, L.; Luo, D.; Fan, W.; Huo, N.; Li, J. Anti-ambipolar behavior and photovoltaic effect in p-$MoTe_2$/n-InSe heterojunctions. *J. Mater. Chem. C* **2021**, *9*, 10372.
(27) Feng, W.; Jin, Z.; Yuan, J.; Zhang, J.; Jia, S.; Dong, L.; Yoon, J.; Zhou, L.; Vajtai, R.; Tour, J. M.; et al. A fast and zero-biased photodetector based on GaTe−InSe vertical 2D p−n heterojunction. *2D Mater.* **2018**, *5*, No. 025008.
(28) Yu, M. M.; Gao, F.; Hu, Y. X.; Wang, L. F.; Hu, P. A.; Feng, W. Tunable electronic properties of multilayer InSe by alloy engineering for high performance self-powered photodetector. *J. Colloid Interface Sci.* **2020**, *565*, 239−244.
(29) Lei, S. D.; Wen, F. F.; Ge, L. H.; Najmaei, S.; George, A.; Gong, Y. J.; Gao, W. L.; Jin, Z. H.; Li, B.; Lou, J.; Kono, J.; Vajtai, R.; Ajayan, P.; Halas, N. J. An Atomically Layered InSe Avalanche Photodetector. *Nano Lett.* **2015**, *15*, 3048−3055.
(30) Yang, Y. J.; Jeon, J.; Park, J. H.; Jeong, M. S.; Lee, B. H.; Hwang, E.; Lee, S. Plasmonic Transition Metal Carbide Electrodes for High-Performance InSe Photodetectors. *ACS Nano* **2019**, *13*, 8804−8810.
(31) Gao, A. Y.; Lai, J. W.; Wang, Y. J.; Zhu, Z.; Zeng, J. W.; Yu, G. L.; Wang, N. Z.; Chen, W. C.; Cao, T. J.; Hu, W. D.; Sun, D.; Chen, X.; Miao, F.; Shi, Y.; Wang, X. Observation of ballistic avalanche phenomena in nanoscale vertical InSe/BP heterostructures. *Nat. Nanotechnol.* **2019**, *14*, 217−222.
(32) Hu, S.; Luo, X.; Xu, J.; Zhao, Q.; Cheng, Y.; Wang, T.; Jie, W.; Castellanos-Gomez, A.; Gan, X.; Zhao, J. Reconfigurable InSe Electronics with van der Waals Integration. *Adv. Electron. Mater.* **2022**, *8*, No. 2101176.
(33) Yan, Y.; Li, S.; Du, J.; Yang, H.; Wang, X.; Song, X.; Li, L.; Li, X.; Xia, C.; Liu, Y.; et al. Reversible Half Wave Rectifier Based on 2D InSe/GeSe Heterostructure with Near-Broken Band Alignment. *Adv. Sci.* **2021**, *8*, No. 1903252.
(34) Huang, Y. T.; Chen, Y. H.; Ho, Y. J.; Huang, S. W.; Chang, Y. R.; Watanabe, K.; Taniguchi, T.; Chiu, H. C.; Liang, C. T.; Sankar, R.; Chou, F. C.; Chen, C. W.; Wang, W. H. High-Performance InSe Transistors with Ohmic Contact Enabled by Nonrectifying Barrier-Type Indium Electrodes. *ACS Appl. Mater. Interfaces* **2018**, *10*, 33450−33456.
(35) Arora, H.; Jung, Y.; Venanzi, T.; Watanabe, K.; Taniguchi, T.; Hubner, R.; Schneider, H.; Helm, M.; Hone, J. C.; Erbe, A. Effective Hexagonal Boron Nitride Passivation of Few-Layered InSe and GaSe to Enhance Their Electronic and Optical Properties. *ACS Appl. Mater. Interfaces* **2019**, *11*, 43480−43487.
(36) Feng, W.; Zheng, W.; Cao, W.; Hu, P. Back gated multilayer InSe transistors with enhanced carrier mobilities via the suppression of carrier scattering from a dielectric interface. *Adv. Mater.* **2014**, *26*, 6587.
(37) Segura, A.; Pomer, F.; Cantarero, A.; Krause, W.; Chevy, A. Electron scattering mechanisms in n-type indium selenide. *Phys. Rev. B* **1984**, *29*, 5708.
(38) Chen, L.; Yu, Z. G.; Liang, D.; Li, S.; Tan, W. C.; Zhang, Y.-W.; Ang, K.-W. Ultrasensitive and robust two-dimensional indium selenide flexible electronics and sensors for human motion detection. *Nano Energy* **2020**, *76*, No. 105020.
(39) Wang, F.; Jiang, J.; Liu, Q.; Zhang, Y.; Wang, J.; Wang, S.; Han, L.; Liu, H.; Sang, Y. Piezopotential gated two-dimensional InSe field-effect transistor for designing a pressure sensor based on piezotronic effect. *Nano Energy* **2020**, *70*, No. 104457.
(40) Zhang, L.; Li, Z.; Liu, J.; Peng, Z.; Zhou, J.; Zhang, H.; Li, Y. Optoelectronic Gas Sensor Based on Few-Layered InSe Nanosheets for NO_2 Detection with Ultrahigh Antihumidity Ability. *Anal. Chem.* **2020**, *92*, 11277−11287.

https://doi.org/10.1021/acs.jpcc.3c03390
J. Phys. Chem. C 2023, 127, 16132−16147

(41) Zheng, W.; Yang, C.; Li, Z.; Xie, J.; Lou, C.; Lei, G.; Liu, X.; Zhang, J. Indium selenide nanosheets for photoelectrical NO_2 sensor with ultra sensitivity and full recovery at room temperature. *Sens. Actuators, B* **2021**, *329*, No. 129127.
(42) Tang, Y.; Lei, P.; Liao, K.; Jiang, T.; Chen, S.; Xie, Q.; Luo, W.; Zhao, Y.; Jie, W. Observation of nonvolatile resistive switching behaviors in 2D layered InSe nanosheets through controllable oxidation. *Appl. Phys. Lett.* **2021**, *119*, No. 133103.
(43) Lu, Y. Y.; Peng, Y. T.; Huang, Y. T.; Chen, J. N.; Jhou, J.; Lan, L. W.; Jian, S. H.; Kuo, C. C.; Hsieh, S. H.; Chen, C. H.; Sankar, R.; Chou, F. C. Engineering an Indium Selenide van der Waals Interface for Multilevel Charge Storage. *ACS Appl. Mater. Interfaces* **2021**, *13*, 4618−4625.
(44) Yang, F. S.; Li, M.; Lee, M. P.; Ho, I. Y.; Chen, J. Y.; Ling, H.; Li, Y.; Chang, J. K.; Yang, S. H.; Chang, Y. M.; et al. Oxidation-boosted charge trapping in ultra-sensitive van der Waals materials for artificial synaptic features. *Nat. Commun.* **2020**, *11*, 2972.
(45) Wang, J.; Yu, H.; Hou, C. High-efficiency ternary polymer solar cells with optimized morphology of active layers enabled byfew-layered β-InSe nanosheets. *Nanoscale* **2021**, *13*, 6871.
(46) Imai, K.; Suzuki, K.; Haga, T.; Hasegawa, Y.; Abe, Y. Phase diagram of In-Se system and crystal growth of indium monoselenide. *J. Cryst. Growth* **1981**, *54*, 501−506.
(47) Wang, Y.; Gao, J.; Wei, B.; Han, Y.; Wang, C.; Gao, Y.; Liu, H.; Han, L.; Zhang, Y. Reduction of the ambient effect in multilayer InSe transistors and a strategy toward stable 2D-based optoelectronic applications. *Nanoscale* **2020**, *12*, 18356−18362.
(48) Fitzgerald, A. G. The crystallization and decomposition on InSe thin films. *Thin Solid Films* **1972**, *13*, S5−S8.
(49) Hossain, J.; Julkarnain, M.; Sharif, K. S.; Khan, K. A. Crystallization of e-beam evaporated amorphous InSe thin films after heat-treatment. *Int. J. Renew. Energy Technol. Res.* **2013**, *2*, 220−226.
(50) Svoboda, R.; Kincl, M.; Málek, J. Thermal characterization of Se-Te thin films. *J. Alloys Compd.* **2015**, *644*, 40−46.
(51) Svoboda, R.; Brandová, D. Crystal growth from mechanically induced defects: A phenomenon observed for glassy materials. *J. Therm. Anal. Calorim.* **2017**, *127*, 799−808.
(52) Svoboda, R.; Prikryl, J.; Provotorov, P.; Kolobov, A. V.; Krbal, M. Next-gen approach to the combined micro/macro-scopic measurements of crystal growth in chalcogenide thin films: The case of Se90Te10. *J. Alloys Compd.* **2022**, *923*, No. 166389.
(53) Svoboda, R.; Prikryl, J.; Kolobov, A. V.; Krbal, M. Preparation of Sb2Se3-based ceramics and glass-ceramics from native thin films deposited on Kapton foil. *Ceram. Int.* **2022**, *48*, 17065−17075.
(54) Svoboda, R.; Prikryl, J.; Cicmancova, V.; Prokop, V.; Kolobov, A. V.; Krbal, M. Crystal Growth in Amorphous Selenium Thin Films—Reviewed and Revisited: Direct Comparison of Microscopic and Calorimetric Measurements. *Cryst. Growth Des.* **2021**, *21*, 7087−7097.
(55) Shahi, S. Flexible optoelectronics. *Nat. Photon.* **2010**, *4*, 506.
(56) Li, H.; Cao, Y.; Wang, Z.; Feng, X. Flexible and stretchable inorganic optoelectronics. *Opt. Mater. Express* **2019**, *9*, 4023−4049.
(57) Li, G.; Zhu, R.; Yang, Y. Polymer solar cells. *Nat. Photon* **2012**, *6*, 153−161.
(58) Carron, R.; Nishiwaki, S.; Feurer, T.; Hertwig, R.; Avancini, E.; Löckinger, J.; Yang, S.; Buecheler, S.; Tiwari, A. N. Advanced alkali treatments for high-efficiency $Cu(In,Ga)Se_2$ solar cells on flexible substrates. *Adv. Energy Mater.* **2019**, *9*, No. 1900408.
(59) Angell, C. A. Formation of glasses from liquids and biopolymers. *Science* **1995**, *267*, 1924−1935.
(60) Angell, C. A. Entropy and fragility in supercooled liquids. *J. Res. Natl. Inst. Stand. Technol.* **1997**, *102*, 171.
(61) Teena, M.; Kunjomana, A. G. Crystal shape engineering and studies on the performance of vapour deposited InSe platelets. *J. Mater. Sci.* **2018**, *29*, 5536−5547.
(62) Hrubý, A. Evaluation of glass-forming tendency by means of DTA. *Czech. J. Phys.* **1972**, *22*, 1187.
(63) Svoboda, R. Crystallization kinetics in Se-Te glassy system - effect of long-term material degradation. *Thermochim. Acta* **2016**, *639*, 108−119.
(64) Svoboda, R. Oxidation-accelerated crystallization of $(GeS_2)_y(Sb_2S_3)_{1-y}$ chalcogenide glasses. *J. Non-Cryst. Sol.* **2017**, *456*, 88−94.
(65) Brandová, D.; Svoboda, R.; Olmrová Zmrhalová, Z.; Chovanec, J.; Bulánek, R. Crystallization kinetics of glassy materials: the ultimate complexity? *J. Therm. Anal. Calorim.* **2018**, *134*, 825−834.
(66) Svoboda, R.; Málek, J. How nucleation-growth kinetics is influenced by initial degree of material crystallinity. *Thermochim. Acta* **2016**, *631*, 28−35.
(67) Svoboda, R.; Málek, J. Evaluation of glass-stability criteria for chalcogenide glasses: Effect of experimental conditions. *J. Non-Cryst. Sol.* **2015**, *413*, 39−45.
(68) Yang, Z.; Jie, W.; Mak, C. H.; Lin, S.; Lin, H.; Yang, X.; Yan, F.; Lau, S. P.; Hao, J. Wafer-Scale Synthesis of High-Quality Semiconducting Two-Dimensional Layered InSe with Broadband Photoresponse. *ACS Nano* **2017**, *11*, 4225−4236.
(69) Emery, J. Y.; Brahim-Otsmane, L.; Jouanne, M.; Julien, C.; Balkanski, M. Growth conditions of InxSey films by molecular beam deposition. *Mater. Sci. Eng. B* **1989**, *3*, 13−17.
(70) Julien, C.; Khelfa, A.; Benramdane, N.; Guesdon, J. P. Preparation and characterization of In_4Se_3 films. *Mater. Sci. Eng. B* **1994**, *27*, 53−60.
(71) Balakrishnan, N.; Steer, E. D.; Smith, E. F.; Kudrynskyi, Z. R.; Kovalyuk, Z. D.; Eaves, L.; Patanè, A.; Beton, P. H. Epitaxial growth of γ-InSe and α, β, and γ-In2Se3 on ε-GaSe. *2D Mater.* **2018**, *5*, No. 035026.
(72) Bergeron, H.; Guiney, L. M.; Beck, M. E.; Zhang, C.; Sangwan, V. K.; Torres-Castanedo, C. G.; Gish, J. T.; Rao, R.; Austin, D. R.; Guo, S.; et al. Large-area optoelectronic-grade InSe thin films via controlled phase evolution. *Appl. Phys. Rev.* **2020**, *7*, No. 041402.
(73) Okamoto, H. In-Se (indium-selenium). *J. Phase Equilibr. Diffus.* **2004**, *25*, 201.
(74) Ward, T. Molecular Structure of Dilute Vitreous Selenium-Sulfur and Selenium-Tellurium Alloys. *J. Phys. Chem.* **1970**, *74*, 4110−4115.
(75) Yannopoulos, S. N. Structure and photo-induced effects in elemental chalcogens: a review on Raman scattering. *J. Mater. Sci.* **2020**, *31*, 7565−7595.
(76) Gan, J.; Lu, X.; Wu, J.; et al. Oxygen vacancies promoting photoelectrochemical performance of In_2O_3 nanocubes. *Sci. Rep.* **2013**, *3*, 1021.
(77) Panda, R.; Naik, R.; Mishra, N. C. Low-temperature growth of γ phase in thermally deposited In_2Se_3 thin films. *Phase Transitions* **2018**, *91*, 862−871.
(78) Weszka, J.; Daniel, P.; Burian, A.; Burian, A. M.; Nguyen, A. T. Raman scattering in In2Se3 and InSe2 amorphous films. *J. Non-Cryst. Solids* **2000**, *265*, 98−104.
(79) Waghmare, A.; Sharma, V.; Shinde, P.; et al. Preparation and characterization of γ-In_2Se_3 thin-film photoanodes for photoelectrochemical water splitting. *J. Solid State Electrochem.* **2022**, *26*, 219−232.
(80) Lewandowska, R.; Bacewicz, R.; Filipowicz, J.; Paszkowicz, W. Raman scattering in α-In2Se3 crystals. *Mater. Res. Bull.* **2001**, *36*, 2577−2583.
(81) Jabłońska, A.; Burian, A. Separation of vibrational and static disorder in amorphous In−Se films by EXAFS. *J. Alloys Compd.* **2004**, *382*, 211−217.
(82) Zargarova, M. I.; Babaeva, P. K.; Azhdarova, D. S.; Melikova, Z. D.; Mekhtieva, S. A. A Study of the Systems CuInSe∼2∼-InSe (SnSe∼2∼, Bi∼2∼Se∼3∼). *Inorg. Mater.* **1995**, *31*, 263−264.
(83) Grzeta, B.; Popovic, S.; Cowlam, N.; Celustka, B. Low-temperature X-ray diffraction examination of In∼2∼Se∼3∼. *J. Appl. Crystallogr.* **1990**, *23*, 340−341.
(84) Krbal, M.; Kolobov, A. V.; Hyot, B.; André, B.; Fons, P.; Simpson, R. E.; Uruga, T.; Tanida, H.; Tominaga, J. Amorphous InSb:

Longer bonds yet higher density. *J. Appl. Phys.* **2010**, *108*, No. 023506.
(85) Tool, A. Q. Relation between inelastic deformability and thermal expansion of glass in its annealing range. *J. Am. Ceram. Soc.* **1946**, *29*, 240−253.
(86) Narayanaswamy, O. S. A Model of Structural Relaxation in Glass. *J. Am. Ceram. Soc.* **1971**, *54*, 491−498.
(87) Moynihan, C. T.; Easteal, A. J.; De Bolt, M. A.; Tucker, J. Dependence of the Fictive Temperature of Glass on Cooling Rate. *J. Am. Ceram. Soc.* **1976**, *59*, 12−16.
(88) Svoboda, R. Utilization of "q^+/q^- = const." DSC cycles for enthalpy relaxation studies. *Eur. Polym. J.* **2014**, *59*, 180−188.
(89) Svoboda, R. Novel equation to determine activation energy of enthalpy relaxation. *J. Therm. Anal. Calorim.* **2015**, *121*, 895−899.
(90) Svoboda, R.; Čičmanec, P.; Málek, J. Kissinger equation versus glass transition phenomenology. *J. Therm. Anal. Cal.* **2013**, *114*, 285−293.
(91) Svoboda, R.; Málek, J. Glass transition in polymers: (in)correct determination of activation energy. *Polymer* **2013**, *54*, 1504−1511.
(92) Vyazovkin, S.; Burnham, A. K.; Criado, J. M.; Pérez-Maqueda, L. A.; Popescu, C.; Sbirrazzuoli, N. ICTAC Kinetics Committee recommendations for performing kinetic computations on thermal analysis data. *Thermochim. Acta* **2011**, *520*, 1−19.
(93) Scherer, G. W. *Relaxation in Glass and Composites (Chapter 9)*; John Wiley & Sons: New York, 1986.
(94) Šesták, J. *Science of Heat and Thermophysical Studies: A Generalized Approach to Thermal Analysis*; Elsevier: Amsterdam, 2005.
(95) Šesták, J. *Thermophysical Properties of Solids, Their Measurements and Theoretical Analysis*; Elsevier: Amsterdam, the Netherlands, 1984.
(96) Opfermann, J. Kinetic analysis using multivariate non-linear regression. *J. Therm. Anal. Calorim.* **2000**, *60*, 641−658.
(97) Svoboda, R.; Chovanec, J.; Slang, S.; Beneš, L.; Konrád, P. Single-curve multivariate kinetic analysis: Application to the crystallization of commercial Fe-Si-Cr-B amorphous alloys. *J. Alloys Compd.* **2021**, *889*, No. 161672.
(98) Kissinger, H. E. Reaction Kinetics in Differential Thermal Analysis. *Anal. Chem.* **1957**, *29*, 1702−1706.
(99) DuPont Kapton® datasheet − accessible at: https://www.dupont.com
(100) Dmitriev, A. I.; Kaminskiĭ, V. M.; Lashkarev, G. V.; Butorin, P. E.; Kovalyuk, Z. D.; Ivanov, V. I.; Beskrovnyĭ, A. I. Neutron Diffraction Studies of the Negative Thermal Expansion in a Layered Indium Selenide Crystal. *Phys. Solid State* **2009**, *51*, 2342−2346.
(101) Svoboda, R.; Málek, J. Interpretation of crystallization kinetics results provided by DSC. *Thermochim. Acta* **2011**, *526*, 237−251.
(102) Svoboda, R. Crystallization of glasses − When to use the Johnson-Mehl-Avrami kinetics? *J. Eur. Ceram. Soc.* **2021**, *41*, 7862−7867.
(103) Avrami, M. Kinetics of phase change I − General theory. *J. Chem. Phys.* **1939**, *7*, 1103−1112.
(104) Avrami, M. Kinetics of phase change. II − Transformation-time relations for random distribution of nuclei. *J. Chem. Phys.* **1940**, *8*, 212−224.
(105) Avrami, M. Granulation, phase change, and microstructure − Kinetics of phase change III. *J. Chem. Phys.* **1941**, *9*, 177−184.
(106) Johnson, W. A.; Mehl, K. F. Reaction kinetics in processes of nucleation and growth. *Trans. Metall. Soc. AIME* **1939**, *135*, 416−442.

https://doi.org/10.1021/acs.jpcc.3c03390
J. Phys. Chem. C 2023, 127, 16132−16147